Article

Utilizing Energy Transfer in Mn²⁺/Ho³⁺/Yb³⁺ Tri-doped ZnAl₂O₄ Nanophosphors for Tunable Luminescence and Highly Sensitive Visual Cryogenic Thermometry

Annu Balhara, Santosh Kumar Gupta,* Anil Krishna Debnath, and Kathi Sudarshan

Cite This: *ACS Omega* 2023, 8, 30459−30473

Read Online

ACCESS | Metrics & More | Article Recommendations | SI Supporting Information

ABSTRACT: Lanthanide (Ln³⁺)-doped upconversion (UC) phosphors converting near-infrared (NIR) light to visible light hold very high promise toward biomedical applications. The scientific findings on luminescent thermometers revealed their superiority for noninvasive thermal sensing. However, only few reports showcase their potential for applications in extreme conditions (temperatures below −70 °C) restricted by low thermal sensitivity. Here, we demonstrate the tailoring of luminescence properties via introducing Ho³⁺−Mn²⁺ energy transfer (ET) routes with judicious codoping of Mn²⁺ ions in ZnAl₂O₄/Ho³⁺,Yb³⁺ phosphor. Preferentially, a singular red UC emission is required to improve the bioimaging sensitivity and minimize tissue damage. We could attain UC emission with 94% red component by a two-photon UC process. Higher temperature annealing brings the color coordinates to the green domain, highlighting the potential for color-tunable luminescence switch. Moreover, this work investigates the thermometric properties of ZnAl₂O₄/Yb³⁺, Ho³⁺ in the range of 80−300 K and influence of inducing extra ET pathways by Mn²⁺ codoping. Interestingly, the luminescence intensities for nonthermally coupled ($^5F_4,^5S_2$) and the $^5F_5$ radiative transitions of Ho³⁺ ions display opposite behavior at 80 and 300 K, which revealed competition between temperature-sensitive decay pathways. The codoping of Mn²⁺ ions is fruitful in causing a fourfold increase of absolute sensitivity. Notably, the color tunability from green through yellow to red is helpful in rough temperature estimation by naked eyes. The maximum relative (S_r) and absolute sensitivities (S_a) were estimated to be 1.89% K⁻¹ (140 K) and 0.0734 K⁻¹ (300 K), respectively. Even at 80 K, a S_a of 0.00447 K⁻¹ and S_r of 0.6025% K⁻¹ were achievable in our case, which are higher than most of the other Ln³⁺-based systems. The above-mentioned results demonstrate the potential of ZnAl₂O₄/Yb³⁺,Ho³⁺ for cryogenic optical thermometry and a strategy to design new Ln³⁺-based UC thermometers by taking advantage of ET routes.
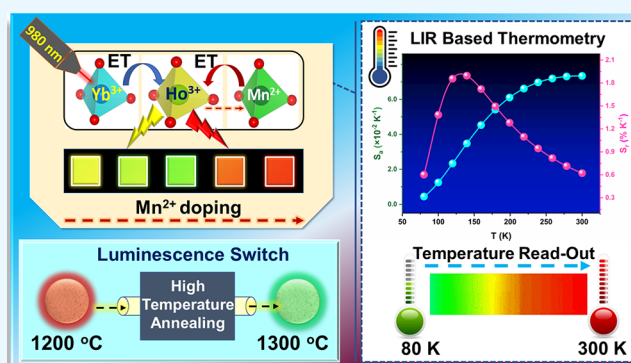
1. INTRODUCTION

Upconversion (UC) materials have garnered global attention of researchers due to their applications in the field of bioimaging, image-guided cancer therapy, luminescence thermometry, solid-state lighting, and anti-counterfeiting.[1−9] In the past decades, lanthanide (Ln³⁺)-doped phosphors emerged as potential UC materials on account of their high photostability, large anti-Stokes shift, longer lifetimes, sharp tunable emissions, and ladder-like 4f energy levels. The use of near-infrared (NIR) excitations lying in the "optical transparency window" of biological tissues (usually 700−1100 nm) is promising for bioapplications and has several well-known merits over downconversion (DC) materials such as deep tissue penetration, less autofluorescence, safe to DNA and tissues, and lower phototoxicity.[1,4,9]

Among lanthanides, Er³⁺, Tm³⁺, and Ho³⁺ ions are typically utilized as activator ions in UC phosphors and generally exhibit UC visible emissions consisting of both green and red emission

bands along with weak blue emissions.[10−13] The green emission has lower escaping tendency from tissues and may generate autofluorescence that lowers the spatial resolution and thus is undesirable.[14,15] The singular red UC emission is essential for high bioimaging sensitivity owing to the large penetration depth, high escape tendency in tissues, and less light scattering.[16−18] Many efforts have been made to achieve the ideal single-component red UC emission of the Er³⁺−Yb³⁺ and Ho³⁺−Yb³⁺ sensitizer−activator pair by tailoring the luminescence properties using strategies such as optimization of synthetic methods, tuning sensitizer doping concentrations,

and NIR pump power modulation and inducing specific pathways for energy transfer (ET) via codoping of other ions. Fortunately, the relaxation dynamics of activator lanthanide ions could be influenced by inclusion of other dopant ions such as Cr^{3+}, Mn^{2+}, Mn^{4+}, Zr^{4+}, Mg^{2+}, Ce^{3+}, or Gd^{3+} in the host lattice.[14−19] For example, Giordano et al.[15] reported enhanced red-UCL with incorporation of Ce^{3+} ions in the $NaBiF_4$/Yb^{3+}/Ho^{3+} phosphor, Rai et al.[16] utilized codoping of Gd^{3+} to enhance red UC in the Er^{3+}/Yb^{3+} system, Srivastava et al.[17] reported a single red emission facilitated by $Er^{3+} \rightarrow Cr^{3+}$ ET, and Tian et al.[19] showcased the manipulation of red and green UC emissions via codoping of Mn^{2+} ions in the $NaYF_4$: Er^{3+}/Yb^{3+} system. However, there are several issues associated with these ions such as toxicity concerns with Cr^{3+} ions,[20] ultraviolet emission from Gd^{3+} ions, which may damage the tissue,[21] and Mg^{2+}/Zr^{4+} being nonfluorescent ions cannot be exploited for multifunctional applications such as magnetic resonance imaging (MRI). Ce^{3+} being a rare-earth ion is explicitly used for commercial white light in the form of yellow phosphor (YAG/Ce^{3+}) and needs to be preserved for future lighting. Therefore, the entire focus is on exploring the manganese ion for generating singular red emission in upconvertible phosphors. In recent years, there are many publications exploring the ET between Er^{3+} and Mn^{2+} ions that are useful for attaining color tunability by manipulation of the red-to-green (R/G) ratio.[22−30] However, achieving a single-component red UC emission in Ho^{3+}−Yb^{3+}-based hosts has been very challenging, and there are few reports on the effect of codoping Mn^{2+} in Ho^{3+}/Yb^{3+}-based UC phosphors.[31−34] To be noteworthy, most of the reports have considered the fluoride-based host lattice for studying the Ho^{3+} and Mn^{3+} ET processes in the Yb^{3+}/Ho^{3+}/Mn^{2+} system that may raise safety concerns over long-term biomedical applications.[6] Particularly, the literature for investigating the effect of Mn^{2+} codoping in Ho^{3+}/Yb^{3+}-based oxide host matrices is very limited. In addition, the inclusion of magnetic Mn^{2+} ions in the host matrix is helpful to design a bioprobe that could be suitably utilized for a promising noninvasive magnetic resonance imaging (MRI) technique along with optical imaging for single cells as well as in-depth tissue imaging.[35,36]

In recent years, Ln^{3+}-based upconversion materials have emerged as excellent exploratory materials for remote temperature sensing by using the luminescence intensity ratios (LIR) between two thermally coupled or nonthermally coupled electronic transitions and the studies are well documented.[37] The Ln^{3+} ion-doped luminescence thermometers resolve most of the concerns raised by use of traditional thermometers and offer contactless, high accuracy, high sensitivity in a wide temperature range and provide information even at the nanoscale regime. Ln^{3+} ion-based UC materials have a rich photoluminescence spectrum due to the presence of many electronic transitions between intermediate excited energy levels and exhibit temperature-dependent LIR and decay lifetimes. To improve the sensitivity of optical thermometers, the use of temperature-dependent LIR among the non-thermally coupled levels can be a potential strategy as their energy band gap is not limited as in the case for thermally coupled levels.[24] The Ho^{3+}-doped upconversion luminescent materials can be a promising candidate as numerous options are available for selecting the emission lines for LIR due to a large number of available excited states for the upconversion emission.[38] Many efforts have been made to improve the relative temperature sensitivity of nonthermally coupled levels

in LIR-based optical thermometers.[38] One of the promising strategies to design highly sensitive thermometers is to modulate the populating channels for excited states of Ho^{3+} ions by doping extra ions for initiating more ET pathways that are competitive with multiphonon and nonradiative relaxations. For example, Swieten et al.[39] observed a high relative sensitivity (S_r) of 1.0% K^{-1} at 300 K for LIR between red and green emissions in the Ho^{3+}-based Na(Y,Gd)F_4 thermometer, and Qiang et al.[29] reported the absolute sensitivity (S_a) of 0.199 K^{-1} (523 K) in the $NaGdF_4$:Yb^{3+}/Ho^{3+}/0.4Mn^{2+} system for LIR among red and green emissions. Hence, the use of nonthermally coupled levels and more ET routes for LIR has showcased higher S_r values required to detect a small temperature variation.

However, very few studies investigate the temperature-dependent UC emissions of Ho^{3+}-based upconversion materials below 300 K. Chai et al.[40] obtained the S_a of 0.0064 K^{-1} at 83 K in Ho^{3+}/Yb^{3+}-codoped $ZnWO_4$ phosphors, Li et al.[41] reported 0.0129 K^{-1} S_r value at 156 K in $LiYF_4$:20Yb^{3+}, 1Ho^{3+}, while Peng et al.[24] demonstrated a maximum S_a value of 0.0124 K^{-1} in the KLu_2F_7:Yb^{3+}/Er^{3+}/Mn^{2+} phosphor. Moreover, Wang et al.[42] reported a $Na_{0.5}Bi_{0.5}TiO_3$:Ho^{3+}-based cryogenic temperature sensor with a very low S_a value of 0.09 × 10^{-3} K^{-1} and high S_r of 6.14% K^{-1} at 167 K. In addition, visual optical thermometry will offer the advantage of rough temperature monitoring by naked eyes and facilitate use as sign boards. Lv et al.[13] have developed a Ho^{3+}/Yb^{3+}-codoped $Al_2Mo_3O_{12}$-based visual optical thermometer showing color changes from green to yellow red from 303 to 463 K. Swieten et al.[39] reported the thermochromic properties of a Ho^{3+}-based Na(Y,Gd)F_4 thermometer and demonstrated a strong color shift from red to green in the temperature range of 293−873 K. However, visual color changes for cryogenic temperatures have been reported rarely and can be promising for space and biomedical applications. We strongly believe that such investigations will open a new thermal sensing system suitable for applications in cryogenics.

In our study, we selected a promising oxide-based host, $ZnAl_2O_4$, that has a normal spinel structure, wide band gap, high chemical and thermal stability, and the ability to incorporate most of the transition and rare-earth ions as dopants.[43−45] The objective of our work is to tailor the relaxation dynamics via ET routes by codoping of Mn^{2+} ions in the $ZnAl_2O_4$/Ho^{3+},Yb^{3+} phosphor. The thermally induced tailoring of the R/G ratio of UCL highlighted its potential as a luminescence switch, and color tunability to the red domain presents the potential of the Ho^{3+}/Yb^{3+}/Mn^{2+}-codoped $ZnAl_2O_4$ phosphor for bioapplications. In addition, ET processes were supported by lifetime measurements, and insights into the UC emission mechanism were obtained from laser power dependencies. Furthermore, this work demonstrates the influence of Mn^{2+} doping in the Ho^{3+}/Yb^{3+}-based hosts on temperature-dependent luminescence properties and ET routes below room temperature (RT). Importantly, an attempt was made to achieve singular red UC emission and color-tunable cryogenic thermal sensors by Mn^{2+} codoping and improve the temperature sensing performance of the $ZnAl_2O_4$/ Ho^{3+},Yb^{3+} host lattice below RT.

2. EXPERIMENTAL SECTION

2.1. Synthesis. The $ZnAl_2O_4$:1%Ho^{3+},5%Yb^{3+}, x%Mn^{2+} (x = 0, 0.25, 0.5, 1 and 2 mol %) phosphors were synthesized by using the solid-state method. The stoichiometric weights of

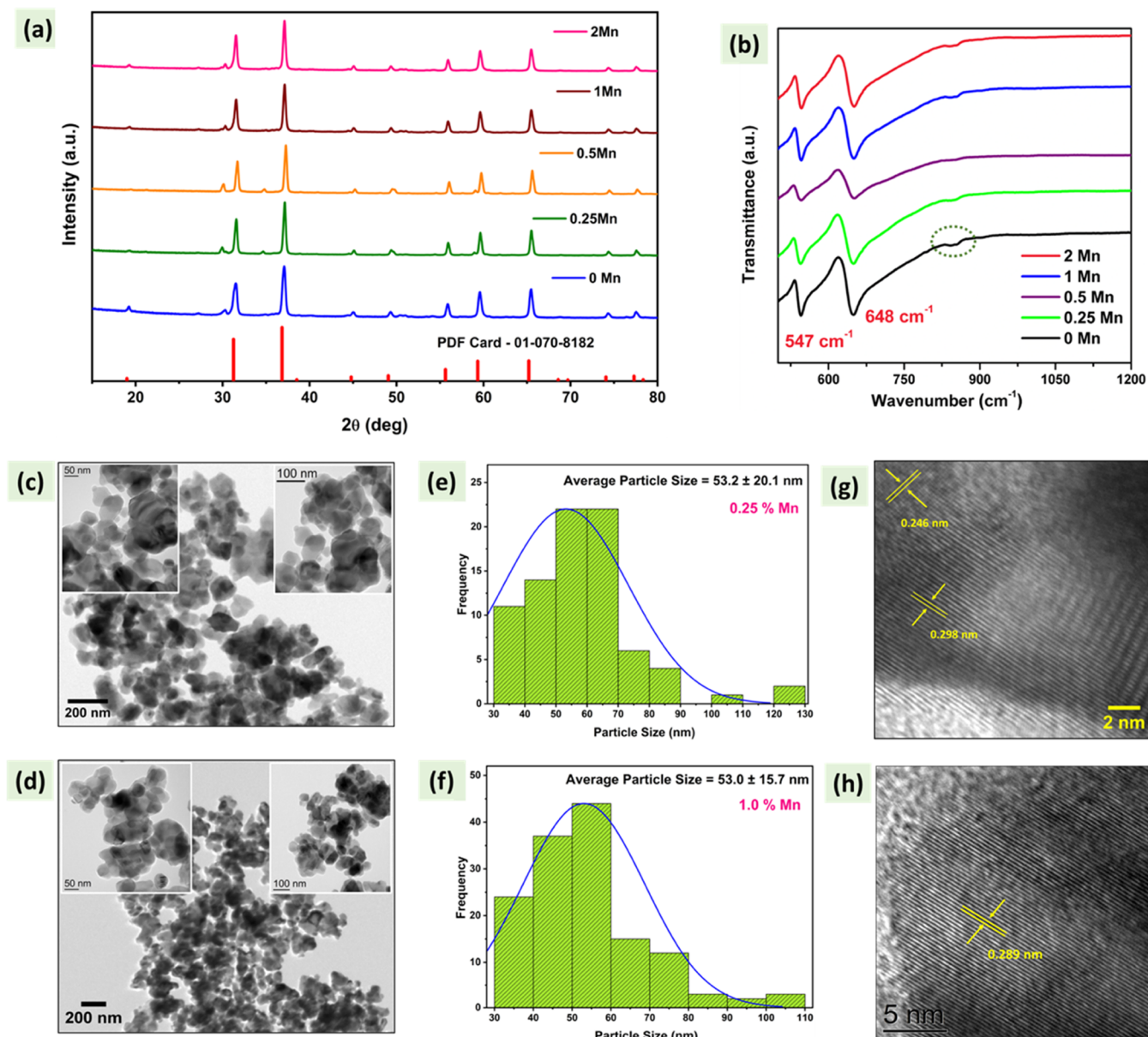**Figure 1.** (a) XRD patterns, (b) FTIR spectra of codoped $ZnAl_2O_4$:1%Ho^{3+},5%Yb^{3+}, x%Mn^{2+} (x = 0, 0.25, 0.5, 1 and 2 mol %) samples; (c, d) TEM images, (e, f) size distribution curves, and (g, h) HR-TEM images of 0.25 and 1.0 mol % Mn^{2+}-codoped sample, respectively.

precursors, ZnO (99.995%), Al_2O_3 (99.995%), Ho_2O_3 (99.995%), Yb_2O_3 (99.99%), and $MnCO_3$ were mixed evenly by grinding using a mortar and pestle. Then, the finely ground samples were calcined at 900 °C for 15 h in a tubular furnace. The grinding of powder was done and further annealed at 1200 °C for 15 h. Finally, the well-ground samples were used for further characterization and measurements. The $ZnAl_2O_4$ sample codoped with 1 mol % of Mn^{2+} ions was annealed at higher temperatures, 1300 and 1400 °C.

2.2. Instrumentation. The powder X-ray diffraction (XRD) patterns of the samples were recorded in the 2θ range of 15−80° on a Proto-AXRD bench top system with a scan rate of 1°/min. Structural and phase analysis was carried out by utilizing Fourier transform infrared spectroscopy (FTIR) that was performed in ATR mode on a Bruker α FTIR spectrometer in the range from 400 to 1200 cm^{-1}. The UC emission spectra were acquired on an FLS1000 fluorescence spectrometer (Edinburgh Instruments, U.K.)

adopting a 980 nm (5 W) laser source operated in C.W. mode for emission spectra and pulse mode for photo-luminescence (PL) decay plots and with photomultiplier tube (PMT) as the detector. Low-temperature dependence studies were also carried out on an FLS-1000 using a cryostat and liquid nitrogen as the coolant. X-ray photoelectron spectroscopy (XPS) measurements were performed with a Mg Kα source having an energy of 1.2356 KeV using a DESA-150 electron analyzer (Staib Instruments, Germany). The morphology studies were performed by using field emission scanning electron microscopy (FE-SEM) (Make: Carl Zeiss, Model: GEMINISEM300). TEM images were recorded with a JEOL, JEM-2100F, and 200 kV electron source. Particle size distribution and d-spacing calculation for HR-TEM images were performed with the help of ImageJ software. EPR spectra were acquired on a Bruker EMX Series spectrometer operated with X band frequency (9.5 GHz) and 100 kHz field modulation. Low-temperature EPR studies were done with
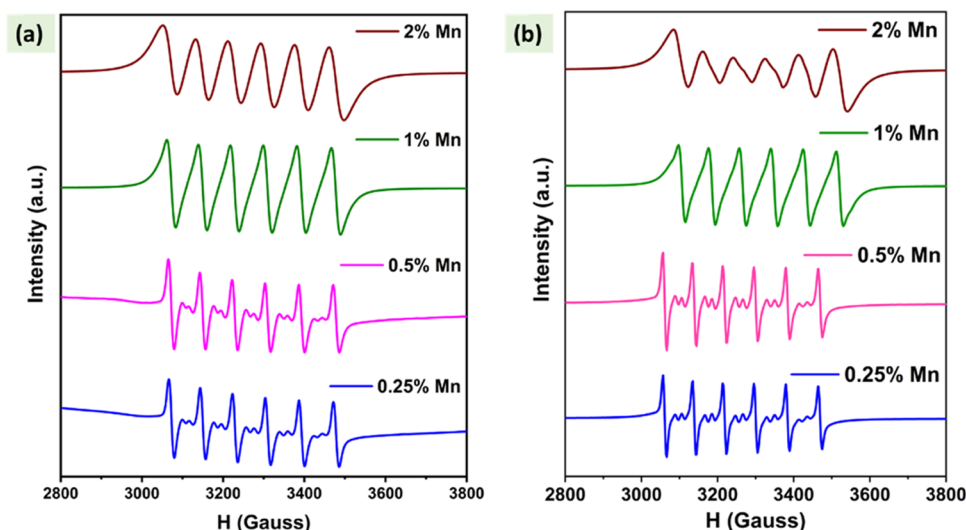
Figure 2. EPR spectra of Mn^{2+}-codoped $ZnAl_2O_4$:1%Ho^{3+},5%Yb^{3+}, x%Mn^{2+} ($x = 0.25, 0.5, 1$ and 2 mol %) samples at (a) room temperature and (b) 100 K.

the help of a BVT 4000 unit using liquid nitrogen along with high-purity "Ar" gas. Positron annihilation lifetime measurements were carried using 10μCi Na-22 deposited between two 8-micron polyimide films as a source of positrons. The source is immersed in the powder sample for acquisition of positron annihilation lifetime spectra using a spectrometer having a resolution of 185 ps. The spectra were analyzed using PALSFit software,[46] which has the provision to account for the spectrometer resolution and fraction of positrons annihilating in the polyimide films encapsulating Na-22.

3. RESULTS AND DISCUSSION

3.1. Phase, Structural, and Morphological Analysis.
Figure 1a presents the XRD patterns of $ZnAl_2O_4$:1%Ho^{3+},5%Yb^{3+}, x%Mn^{2+} ($x = 0, 0.25, 0.5, 1$ and 2 mol %) samples. The observed diffraction peaks are due to the formation of $ZnAl_2O_4$ in the cubic spinel phase in all the codoped $ZnAl_2O_4$ samples (PDF Card - 01−070−8182). A feeble peak at $2\theta \sim 30°$ could be attributed to the presence of the Yb_2O_3 residue. Figure S1 (Supporting Information, SI) presents the XRD patterns of the 1 mol % Mn^{2+}-doped sample annealed at different temperatures. There may be a contribution of Ho^{3+} ions doped in the Yb_2O_3 impurity phase in the final UC emissions. To clarify the same, we synthesized a 1 mol % Ho^{3+}-doped Yb_2O_3 sample under similar conditions as for $ZnAl_2O_4$ samples. The XRD pattern of the Yb_2O_3:1% Ho^{3+} sample is shown in Figure S2.

Figure 1b exhibits the FTIR spectrum of all samples. The absorption bands were observed in the range from 400−800 cm^{-1} and can be assigned to the stretching vibrations of Al−O bonds present in the octahedral AlO_6 symmetry.[45] The vibrational bands peaking at 648 and 547 cm^{-1} are due to the symmetric stretching and symmetric bending vibrational modes of the octahedral AlO_6, respectively.[45] Also, a weak shoulder band at ∼848 cm^{-1} marked in circle (Figure 1b) revealed minor inversion in the $ZnAl_2O_4$ normal spinel structure. The FE-SEM images of the $ZnAl_2O_4$:1%Ho^{3+},5%Yb^{3+} sample are presented in Figure S3. The FE-SEM images revealed the formation of small nanospherical grains, in line with TEM results (Figure 1c,d), providing additional inputs that particles are agglomerated together. The agglomerated nanoparticles are formed as a result of annealing at high

temperature. The TEM images of 0.25 and 1.0 mol % Mn^{2+}-codoped samples (Figure 1c,d) show irregular sphere-like morphology of particles and nonuniform size distribution. The size distribution curves (Figure 1e,f) showed no significant changes in particle sizes on increase in the Mn^{2+} codoping concentrations, and the average size of individual grains for 0.25 and 1.0 mol % Mn^{2+}-codoped samples is 53.2 and 53.0 nm, respectively. The lattice fringes in the HR-TEM images of the 0.25 mol % Mn^{2+}-codoped sample (Figure 1g) with a d-spacing of 0.298 and 0.246 nm correspond to the (220) and (311) crystal planes of the cubic $ZnAl_2O_4$ spinel, respectively. The lattice fringes having a d-spacing of 0.289 nm of (220) planes were observed in the HR-TEM images of the 1.0 mol % Mn^{2+}-codoped sample (Figure 1h).

3.2. Manganese Ion Oxidation State: XPS and EPR Study.
To confirm the formation of Mn^{2+}, we performed XPS analysis for the $ZnAl_2O_4$:1%Ho^{3+}, 5%Yb^{3+}, 1%Mn^{2+} sample. Figure S4a,b shows the XPS survey spectrum and XPS spectrum for Mn peaks. The Mn-$2P_{3/2}$ and Mn-$2P_{1/2}$ are observed around 641.1 and 652.8 eV that can be ascribed due to the presence of Mn ions mainly in the valence state of Mn^{2+}.[47] Figure 2a presents the EPR spectra of manganese-codoped $ZnAl_2O_4$:Ho^{3+},Yb^{3+} samples at room temperature that contain the sextet hyperfine structure, which is characteristic of manganese in the divalent state with Mn^{2+} ($3d^5$, $I = 5/2$) having five unpaired electrons ($S = 5/2$).[48] Moreover, the sextet EPR spectra centered at a g value of ∼2.06 at 300 K further confirm the presence of Mn in the divalent state ($g > 2.00$) as EPR signals of Mn^{4+} are usually seen at $g \sim 1.99$.[48,49] EPR results correlated well with the XPS analysis. The g values at room temperature and 100 K are provided in Table S1. In 0.25 and 0.5 mol % of Mn^{2+}-codoped samples, five doublets in between main lines represent the forbidden transitions ($\Delta m \pm 1$, m = nuclear spin magnetic quantum number), observed along with the allowed six transitions ($\Delta m = 0$).[48] However, in 1.0 and 2.0 mol % of Mn^{2+}-codoped samples, only the six allowed transitions are seen. The g values do not vary at RT with different concentrations of Mn^{2+} ions, but the peak width increases with increasing concentrations of Mn^{2+} ions that are a consequence of dipole and exchange interactions between Mn^{2+} ions.
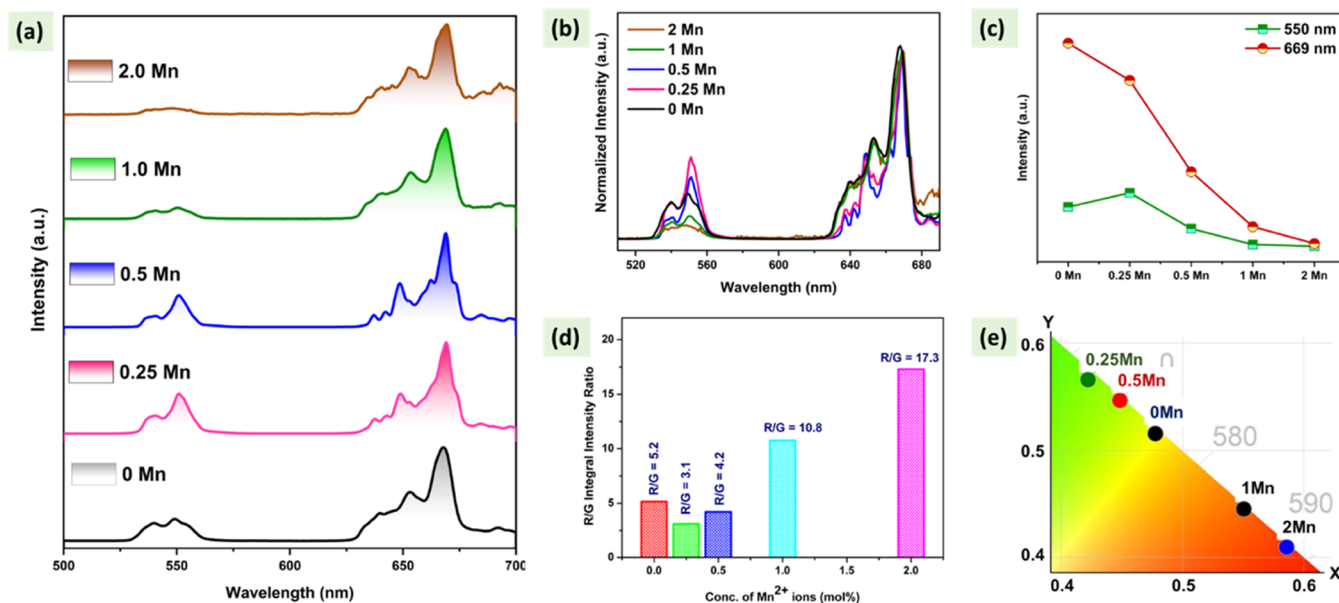
Figure 3. (a) UC emission spectra of codoped $ZnAl_2O_4$:1%Ho^{3+},5%Yb^{3+}, x%Mn^{2+} (x = 0, 0.25, 0.5, 1 and 2 mol %) samples under a 980 nm laser excitation at a laser power of 651 mW, (b) normalized visible UC emission spectra at 669 nm, (c) variation in green and red UCL with the changing codoping concentrations of Mn^{2+} ions, (d) change in R/G ratios with different concentrations of Mn^{2+} ions, and (e) CIE color coordinate diagram of all samples.

The EPR spectra of all Mn^{2+}-codoped samples at 100 K having six hyperfine signals are shown in Figure 2b, and only slight changes in the g values (Figure S5a–d) were observed on decreasing the temperature to 100 K. The low-temperature EPR measurements correspond well with the RT EPR spectra, and g > 2.00 (Table S1) for all the samples confirmed the stabilization of Mn in the divalent state. The more intense EPR signals at 100 K can be ascribed to the increase in the spin population ratio described by Boltzmann distribution. The effect of different annealing temperatures for 1 mol % of Mn^{2+}-codoped sample was analyzed by EPR (Figure S6), and no significant change was observed in g values (Table S2) and peak width that suggests that the environment around Mn^{2+} ions does not change much even on annealing at higher temperatures.

3.3. Defect Evolution: Positron Annihilation Lifetime Measurements. The positron annihilation lifetime spectra in all the cases could be resolved into three lifetime components. The lifetimes are numbered in the increasing order of magnitude. The summary of the positron annihilation lifetimes extracted from the spectra (Figure S7) and intensity-weighted average of the first two positron lifetime components is given in Table S3. The third positron lifetime in the range of ns is due to positronium formation on the surface of the crystallites in the powder samples. The intensity of this component is low in powder samples and is found to be higher if crystallite sizes are smaller.[50] The intensity of the positronium component (I_3) increased with dopants except when a small amount of Mn^{2+} was codoped. The intensity of this component reduced when the sample with 1 mol % of Mn^{2+} was annealed at higher temperature. The ionic radii of Zn^{2+} and Al^{3+} in their respective coordinations are 0.6 and 0.535 Å, respectively. The ionic radii of all the dopants used in the current study are larger than those of both Zn^{2+} and Al^{3+}, but among the dopants, Mn^{2+} is closest in size to Zn^{2+}. Based on the ionic radii of the dopants, it is expected that doping of larger sized

dopants could hinder crystallite growth and cause large distortions in the lattice.[51]

The first positron lifetime (τ_1) in these samples is due to positron annihilation in bulk, but it has contribution from shallow positron traps too as their lifetime is not mathematically decipherable from the bulk lifetime. The second lifetime is due to the vacancy cluster along with contribution from the positron annihilation at the surface of the particles. It is seen from the figure that the intensity of the second positron component is greatly enhanced with doping, which shows increased defects. Doping of Ho^{3+} and Yb^{3+} at Zn^{2+} sites is expected to create charge-compensating defects, which invariably in this case would be zinc vacancies. Although small addition of Mn^{2+}, which is of similar size to Zn^{2+}, marginally reduced this intensity, it is higher in higher Mn^{2+} content samples. The intensity of this second positron component reduced upon annealing the sample of 1 mol % Mn^{2+} at higher temperature. The reduction in the second component could be due to the increase in antisite disorder, which reduced the zinc vacancies that are a result of aliovalent substitution in Zn^{2+} sites. The increase in crystallite sizes is also expected to reduce this intensity via reducing the number positrons reaching the surface or reducing the contribution from surface states to this component.[52] When the 1 mol % Mn^{2+} sample is annealed at 1400 °C, the magnitude of the first lifetime also increased significantly, showing the formation of a larger vacancy cluster or vacancy aggregation. The reduction in the lifetime when a small amount of Mn^{2+} is codoped suggests that a small amount of Mn^{2+} may favor antisite disorder and reduce the charge-compensating vacancies that resulted due to Ho^{3+} and Yb^{3+} doping at Zn^{2+} sites.

3.4. Time-Resolved Photoluminescence. *3.4.1. UC Emissions under 980 nm Laser Excitation.* Figure 3a demonstrates the visible UC emission spectra of $ZnAl_2O_4$:1% Ho^{3+},5%Yb^{3+}, x%Mn^{2+} (x = 0, 0.25, 0.5, 1 and 2 mol %) samples under 980 nm excitations in the region of 500−750 nm. The strong green UC band appearing at (540, 550) nm is
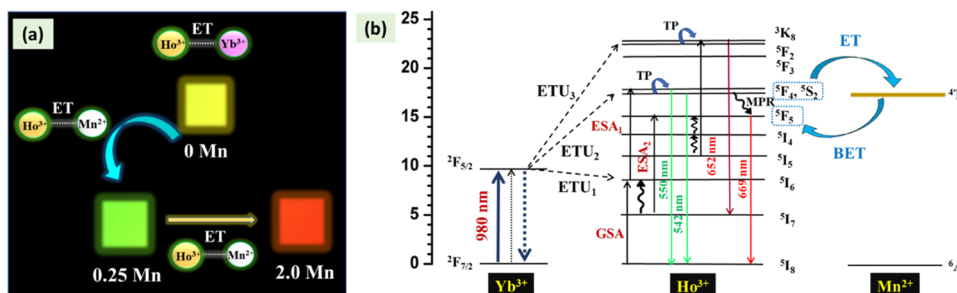
Figure 4. Schematic representation for (a) energy transfer leading to color tunability at different codoping amounts of Mn^{2+} ions and (b) mechanisms of the upconversion and ET processes between Yb^{3+}, Ho^{3+}, and Mn^{2+} ions.

due to radiative decay occurring in $(^5F_4, {}^5S_2) \rightarrow {}^5I_8$ energy levels of Ho^{3+} ions. The intense red UC emission bands positioned at (640, 652) and 669 nm can be assigned to the $(^3K_8, {}^5F_2, {}^5F_3) \rightarrow {}^5I_7$ and ${}^5F_5 \rightarrow {}^5I_8$ transitions, respectively.[12,41,53,54] The strong visible UCL is due to effective energy transfer from Yb^{3+} ions to the Ho^{3+} ions as the Yb^{3+} has a higher absorption coefficient for the 980 nm photons.

After the inclusion of Mn^{2+} ions in the $ZnAl_2O_4$ lattice, alteration in the UC emission intensities of both the green and red emissions was observed as depicted in Figure 3a,b. Figure 3b shows the normalized UCL intensities at 669 nm wavelength and demonstrates changes in green emissions on Mn^{2+} codoping. The splitting of UC emissions depends on the crystal field, and stark splitting of the ${}^5F_5$ level of Ho^{3+} ions may change peak structures in the UC spectra. With different dopings of Mn^{2+} ions, the crystal field may vary and there can be a slight shift in the UC emission spectra. The emission spectra of all samples occupy the same spectral band, and alteration in crystal field splitting resulted in different peak structures. The green and red UC emission intensities depicted a decrease in UCL after codoping of 0.25 mol % of Mn^{2+} samples as the concentration of Mn^{2+} ions increases (Figure 3c). As a result of the changes in the relative radiative probabilities of transitions ascribed to (542, 550), 669, and 652 nm UC emissions, the color tunability from yellow to green to red with increasing concentrations of Mn^{2+} ions could be achieved as can be also schematically visualized in Figure 4a. The changes in the photophysical dynamics of UC can be attributed to the energy transfer (ET) between Mn^{2+} and Ho^{3+} ions.[31-34] The codoping of Mn^{2+} ions induces ET pathways, and thus, the red-to-green UCL ratio (R/G) value increased from 5.2 in the $1\%Ho^{3+} + 5\%Yb^{3+}$-doped sample to 17.3 in the 2 mol % Mn^{2+}-codoped sample (Figure 3d), highlighting its potential for singular red unconvertible materials. We could successfully achieve 94% red emission in the 2 mol % Mn^{2+}-codoped samples in comparison to 84% red emission obtained in the sample without Mn^{2+} ions (Table S4). The color tunability toward red is attainable on changing the codoping concentrations of Mn^{2+} ions and is well presented by the color coordinate diagram in Figure 3e. Figure S8 demonstrates that Ho^{3+} doped in Yb_2O_3 exhibits a feeble UC emission compared to the $ZnAl_2O_4:1\%Ho^{3+},5\%Yb^{3+}$ sample under 980 nm excitation that could be attained only at higher 2.82 W laser power. Thus, strong UC emissions observed in our samples can be ascribed to dopant ions in the major $ZnAl_2O_4$ phase. The same is a consequence of cross-relaxations between Yb^{3+} ions with higher probability in the Yb_2O_3 phase that are competitive with ET from $Yb^{3+} \rightarrow Ho^{3+}$ ions; therefore, ET efficiency can be reduced. However, activator ion doping in the

$ZnAl_2O_4$ phase results in stronger UC emissions because concentration quenching is reduced due to low concentrations of both Ho^{3+} and Yb^{3+} ions.

3.4.2. UC Mechanisms and $Ho^{3+} \rightarrow Mn^{2+}$ Energy Transfer Processes. The Yb^{3+} ions initially present in the ground state $(^2F_{7/2})$ are excited to the excited $^2F_{5/2}$ state after absorption of 980 nm photons. The UC emission in the Ho^{3+}/Yb^{3+} system can occur via the following mechanisms: (i) energy transfer upconversion (ETU), (ii) ground-state absorption (GSA), and (iii) excited-state absorption (ESA).[55] The energy level diagram in Figure 4b depicts the visible UC mechanisms and the possible energy transfer pathways between the Ho^{3+}, Yb^{3+}, and Mn^{2+} ions. The GSA is the most probable mechanism for populating the ${}^5I_6$ excited state of Ho^{3+} ions after the energy is transferred from Yb^{3+} ions due to ETU_1. Since the intermediate levels have higher lifetimes, the Ho^{3+} ions in the ${}^5I_6$ excited state can absorb the photons either by ESA_1 or ETU_2 that result in the green emission on relaxation to the ground state $(^5I_8)$.[54,55] However, the ETU_2 is relatively the more feasible mechanism at lower powers as the ESA requires higher laser powers.[24] The simultaneous multiphonon relaxation (MPR) process can result in the population of the ${}^5F_5$ energy state of Ho^{3+} ions, and radiative decay to the ${}^5I_8$ ground state simulates the emission of 669 nm photons. The MPR from the ${}^5I_6$ state of Ho^{3+} ions and ESA_2 process from the ${}^5I_7$ state can also populate the ${}^5F_5$ energy state.[41] Also, the ${}^5F_5$ energy state of Ho^{3+} ions could be occupied via cross-relaxation (CR), although the probability of this pathway is negligible at low Ho^{3+} ion concentrations.[40] The $(^3K_8, {}^5F_2, {}^5F_3)$ energy levels can be occupied by the ETU_3 process as a result of the nonradiative decay process from the ${}^5F_5$ state to the ${}^5I_5$ energy level of Ho^{3+} ions, and radiative decay from $(^3K_8, {}^5F_2, {}^5F_3)$ energy levels leads to red emissions at 652 and 645 nm.

The codoping of Mn^{2+} ions induces another energy transfer process, where the Ho^{3+} ions excited to the $(^5F_4, {}^5S_2)$ energy state via ETU from Ho^{3+} ion transfer energy to the ${}^4T_1$ energy level of Mn^{2+} ions[32] (represented by blue arrows in Figure 4b). The ET probability between Ho^{3+} and Mn^{2+} ions is high, and this can be attributed to energy matching that leads to effective mixing of their wave functions. As both the Ho^{3+} and Mn^{2+} ions are present in close proximity, the possibility of back energy transfer (BET) processes is also higher and BET may occur from the ${}^4T_1$ energy level of Mn^{2+} ions to the Ho^{3+} ions by nonradiative relaxation to the ground state.[32,34] Interestingly, either the red and green UC emission intensities or one of them could be modulated depending on the host matrices and energy transfer pathways.[31,33,54,55] The BET from the ${}^4T_1$ energy state of Mn^{2+} ions can occur to either of the $(^5F_4, {}^5S_2)$ or ${}^5F_5$ excited levels of Ho^{3+} ions that could selectively enhance

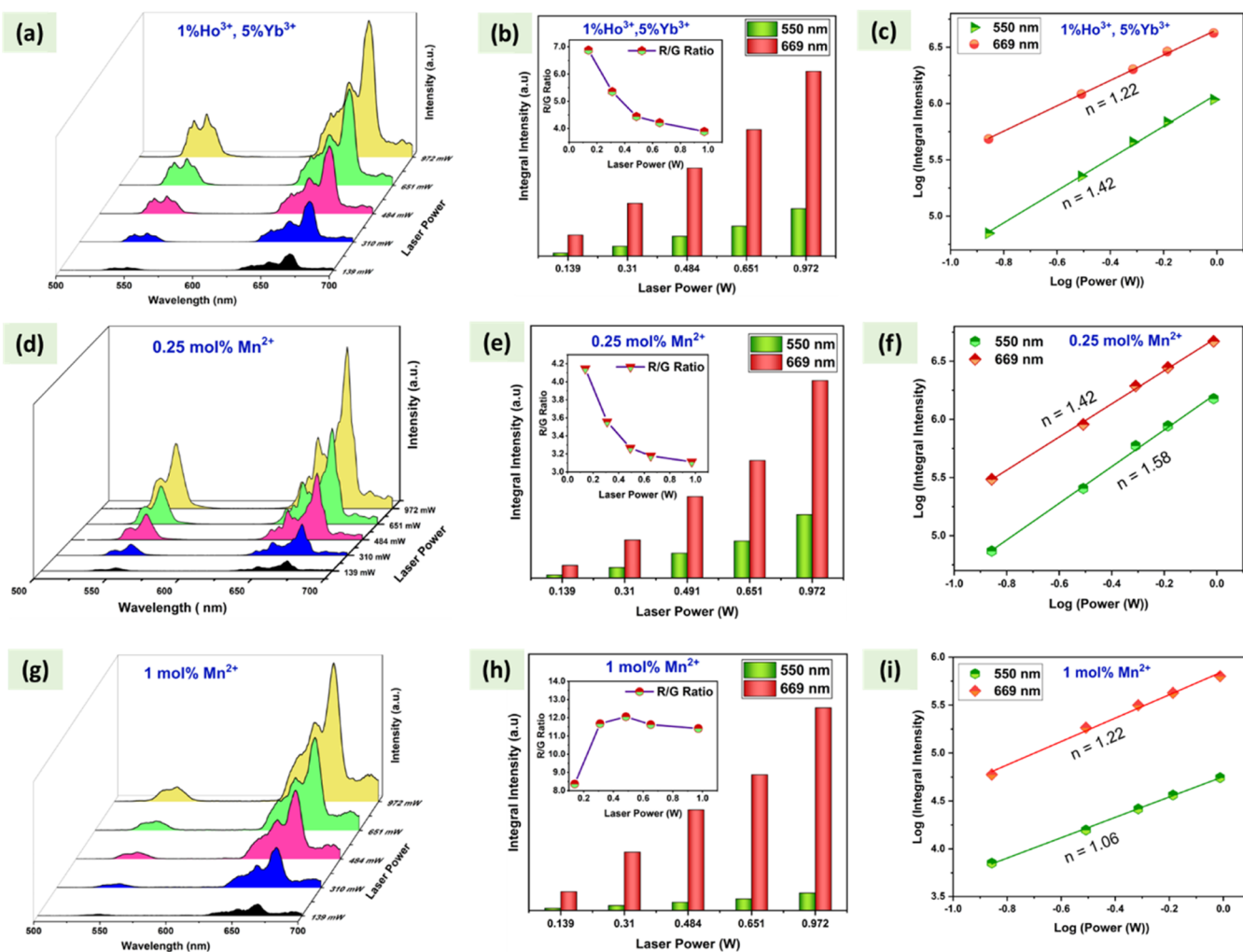**Figure 5.** UC emission laser power dependence of ZnAl$_2$O$_4$:1%Ho^{3+}, 5%Yb^{3+}, x%Mn^{2+}, the R/G ratio change with increasing laser powers, and the dual logarithmic plots between the UC emission integral intensity (550 and 669 nm) and excitation laser power (W), for (a–c) x = 0 mol %, (d–f) x = 0.25 mol %, and (g–i) x = 1 mol % Mn^{2+} ions, respectively.

one of the radiative transitions of Ho^{3+} ions. The increase in the R/G value strongly supports the possible efficient ET between Ho^{3+} and Mn^{2+} ions.

3.4.3. Pump Power Dependence and UC Mechanism Studies. The UC process involves absorption of two or more photons to populate the higher excited state followed by radiative decay to emit high-energy photons. The same mechanism can be understood by investigating the dependencies of UC emission intensities on NIR laser power, and the following relation can be used to find the number of photons (n) involved in the UC mechanism

$$I \propto P^n \tag{1}$$

where I denotes the integral intensity of a UC emission band, P is the power of the pump source, and n is the slope of the logarithmic plot of I vs P.

The enhancement in the emission intensities of both green (550 nm) and red (669 nm) UC emissions was observed on the increase in the NIR laser power for ZnAl$_2$O$_4$: Ho^{3+},Yb^{3+} and ZnAl$_2$O$_4$: Ho^{3+},Yb^{3+},Mn^{2+} samples as demonstrated in Figure 5a,d,g. The change in the red and green UCL with increasing NIR pump powers are demonstrated in Figure 5b,e,h. A decreasing trend in R/G values from 7 to 3.9 and 4.1 to 3 was observed in ZnAl$_2$O$_4$: Ho^{3+},Yb^{3+} and 0.25 mol %

codoped ZnAl$_2$O$_4$: Ho^{3+},Yb^{3+} samples, respectively (inset of Figure 5b,e). Interestingly, in the 1 mol % codoped ZnAl$_2$O$_4$: Ho^{3+},Yb^{3+} sample, the R/G value increased initially with laser power from 8.4 to 12 followed by a decreasing trend (inset of Figure 5h) that may be due to saturation effects. This implies that at higher laser powers, more Ho^{3+} ions are excited to the (^{5}F$_4$,^{5}S$_2$) energy level and efficient ET to Mn^{2+} ions and BET to ^{5}F$_5$ excited levels of Ho^{3+} ions enhance the red UCL relatively to the green UCL. The same observations could be understood by change in color coordinates as a function of NIR laser power for different concentrations of Mn^{2+} ions as depicted in Figure S9a−c.

The dual logarithmic plots of log I vs log P for the 550 nm green and 669 nm red UC emissions are shown in Figure 5c,f,i. The slope values for the red and green UC emissions indicate two-photon absorption for the UC process in the visible region for all the samples. However, the values observed are lower than 2, which may be attributed to saturation effects due to two competing processes, upconversion and luminescence decay to the ground state.[32] The n values for green and red UCL in the ZnAl$_2$O$_4$: Ho^{3+},Yb^{3+} sample are 1.42 and 1.22, respectively, that increased to 1.58 and 1.42 in the 0.25 mol % codoped ZnAl$_2$O$_4$: Ho^{3+},Yb^{3+} sample. Noteworthily, the slope values for green and red UCL in the 1 mol % codoped

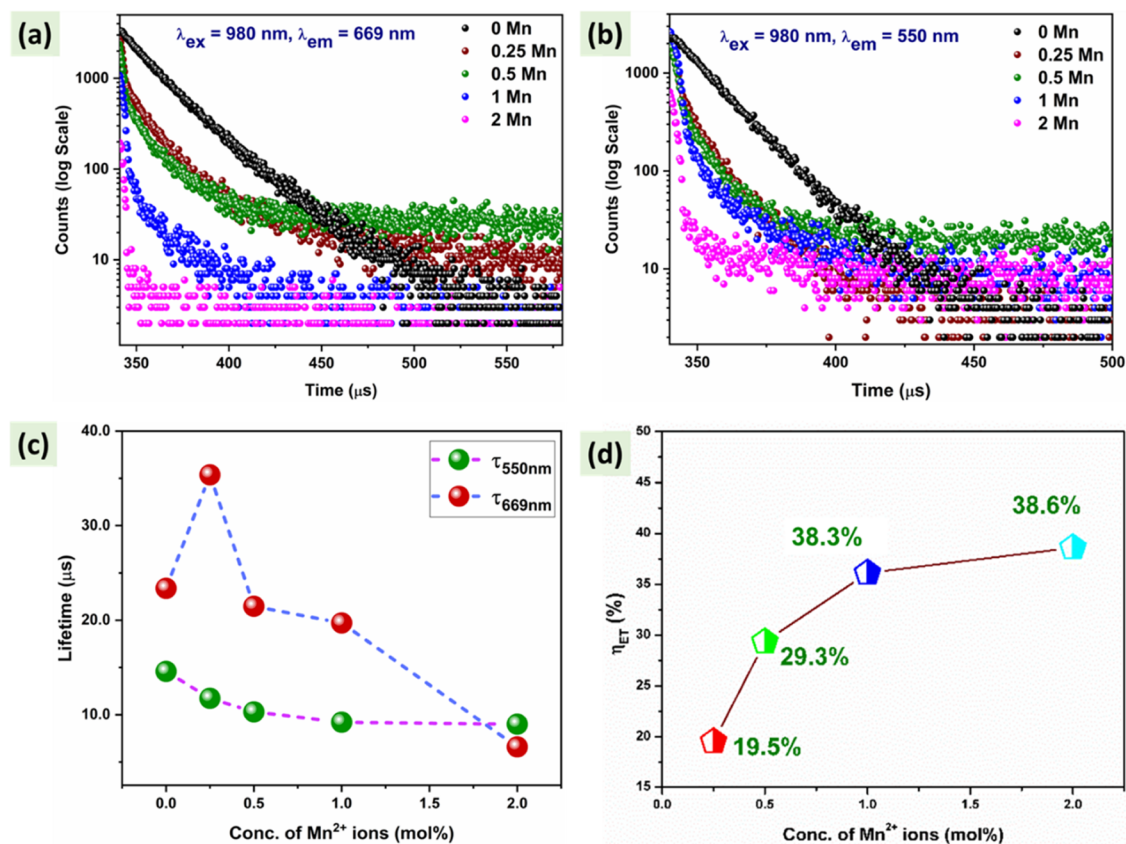**Figure 6.** (a) Luminescence decay profiles of codoped $ZnAl_2O_4$:1%Ho^{3+},5%Yb^{3+}, x%Mn^{2+} (x = 0, 0.25, 0.5, 1 and 2 mol %) samples under 980 nm laser excitation and emission monitored at (a) 669 nm and (b) 550 nm; (c) change in lifetime values with different codoping concentrations of Mn^{2+} ions for UC emissions at 550 and 669 nm, and (d) variation in energy-transfer efficiencies (η_{ET}) with concentrations of Mn^{2+} ions.

$ZnAl_2O_4$: Ho^{3+},Yb^{3+} sample decreased to 1.06 and 1.22, which suggest that a larger upconversion rate and higher doping of Mn^{2+} ions induce more ET that leads to an increased population of Ho^{3+} ions in the excited levels.[24,32] Qiang et al. reported a decrease in slope values on Mn^{2+} codoping in the $NaGdF_4$:Yb/Er system[32] and proposed that Mn^{2+} codoping increased the rate of UC transitions, leading to a smaller slope. Szczeszak et al. observed slope values less than 2 for CaF_2: Yb^{3+}, Er^{3+}, Mn^{2+} and ascribed the same to a larger depopulation rate of intermediate energy levels of Ho^{3+} ions induced by ET and BET processes between Ho^{3+}, Yb^{3+}, and Mn^{2+} ions.[26]

3.4.4. $Mn^{2+} \rightarrow Ho^{3+}$ Ion Energy Transfer Efficiency: Luminescence Decay. The UC decay lifetime of visible UC emissions was measured to gain more insights into the energy transfer process. The decay profile of codoped $ZnAl_2O_4$:1% Ho^{3+},5%Yb^{3+}, x%Mn^{2+} (x = 0, 0.25, 0.5, 1 and 2 mol %) samples monitored at 980 nm laser excitation and emission at 669 and 550 nm is presented in Figure 6a,b, respectively. The biexponential fitting of decay curves of codoped Mn^{2+} samples was performed using the relation

$$I(t) = I_0 + A_1 e^{-t/\tau_1} + A_2 e^{-t/\tau_2} \qquad (2)$$

where $I(t)$ is the UC emission intensity at time t, I_0 is the background intensity at zero offset, A_1 and A_2 are the constants, and τ_1 and τ_2 denote the lifetimes of the fast and slow decays, respectively. The average lifetime values (τ_{av}) for different codoped Mn^{2+} samples for green and red UC emissions are provided in Tables S5 and S6 and are pictorially

represented in Figure 6c. As the concentration of Mn^{2+} ions is increased, the significant decrease in the average lifetimes of Ho^{3+} ions validates the energy transfer between the Ho^{3+} and Mn^{2+} ions. In addition, a single exponential decay in the case of the $ZnAl_2O_4$: Ho^{3+},Yb^{3+} sample without Mn^{2+} ions for both the UC emissions transformed into a biexponential decay. The biexponential decay on inclusion of Mn^{2+} ions reveals the other decay path of Ho^{3+} ions by energy transfer to Mn^{2+} ions.[56] The codoping of Mn^{2+} ions results in crystal field modulation and lowering of symmetry around Ho^{3+} ions that resulted in improved green UCL for the 0.25 mol % Mn^{2+} sample. In addition, energy match between the ($^5F_4$,$^5S_2$) level of Ho^{3+} and $^4T_1$ energy level of Mn^{2+} ions induces ET processes between both dopant ions, which alter the lifetime values. The decreasing lifetime of green emissions is evidence for ET. Mn^{2+} ions in the $^4T_1$ excited state may enhance the population of the $^5F_5$ level by the BET process or undergo nonradiative relaxation processes. The lifetime of emissions from the $^5F_5$ level decreases more significantly due to the presence of ET routes between Mn^{2+} and Ho^{3+} ions. The lifetime of emission from $^5F_5$ of Ho^{3+} ions will be increased if BET occurs efficiently. In our case, an increase in lifetime was significantly observed in the 0.25 mol % Mn^{2+}-doped sample that confirmed the existence of BET. The increase in the decay lifetime of the $^5F_5$ level of Ho^{3+} (τ_{669}) ions from 23.37 to 35.37 μs can be attributed to the back energy transfer (BET) from $^4T_1$ of Mn^{2+} on codoping of 0.25 mol % Mn^{2+} ions (Figure 6c).[57] However, on further increase in Mn^{2+} codoping, a decrease in the τ_{669} was observed as cross-relaxations between dopant ions and
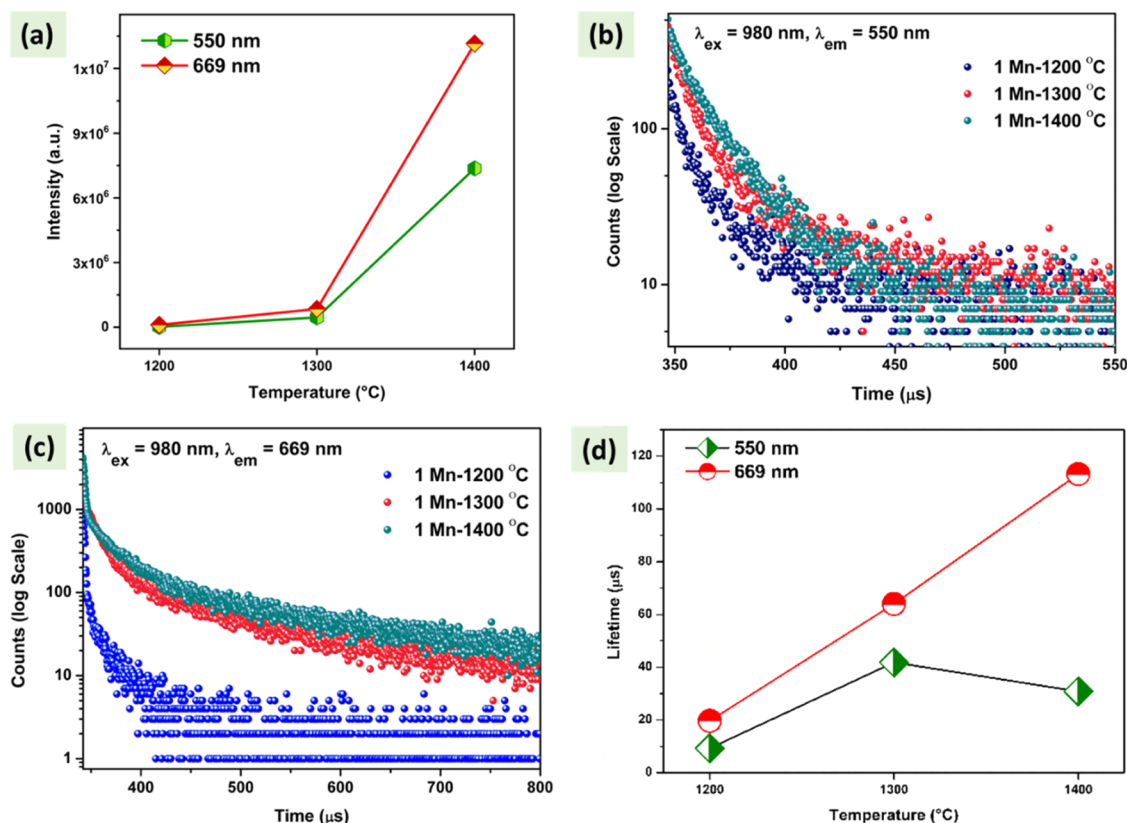
Figure 7. (a) Variation in green and red UCL of the 1 mol % Mn^{2+} ion-codoped $ZnAl_2O_4$ sample annealed at different temperatures; decay curves of Ho^{3+} ions in the 1 mol % Mn^{2+}-codoped sample annealed at different temperatures for (b) 550 nm and (c) 669 nm UC emissions, and (d) variation in lifetimes as a function of annealing temperatures.

nonradiative decay pathways is more probable on higher doping amounts.

The energy transfer rates may vary with the codoping concentrations and distance between Mn^{2+} and Ho^{3+} ions. The energy transfer efficiencies (η_{ET}) were evaluated using the following relation

$$\eta_{ET} = 1 - \frac{\tau_s}{\tau_0} \qquad (3)$$

where τ_s and τ_0 represent the lifetime of Ho^{3+} ions in the presence of Mn^{2+} ions and without Mn^{2+} ions, respectively. The τ_0 for the 550 nm UC emission is 14.59 μs, and τ_s values for different codoped Mn^{2+} samples are tabulated in Tables S5 and S6. The energy transfer efficiency (η_{ET}) increases from 19.5 to 38.6% with an increase in the codoping amounts of Mn^{2+} ions from 0.25 to 2.0 mol % in the $ZnAl_2O_4$: Ho^{3+},Yb^{3+} lattice (Figure 6d).

3.4.5. Effect of Different Annealing Temperatures: UCL and Lifetime Studies. So far, we could achieve success in color tunability and reaching the goal toward singular red emission by modulating the Mn^{2+} concentration but with the cost of reduced emission intensity. To counterbalance the same, we have utilized the strategy of high-temperature annealing of one of the representatives, 1 mol % Mn^{2+} ion-codoped sample. It was found that the UC emission intensities increase with the increase in the annealing temperature (Figure S10a,b). The increase in annealing temperature results in bigger crystallite sizes. However, for $ZnAl_2O_4$, this is predominant at annealing temperatures below 1200 °C. Above 1200 °C, the increase in crystallite size is very gradual. Similar enhancement in PL

intensity has been reported well in the literature where the increase in luminescence enhancement is attributed to decrease in Zn^{2+} cation inversion rate. The same results in reduction of oxygen vacancies forming around Zn_{Al} antisite defects for charge neutrality in the $ZnAl_2O_4$ spinel. Wu et al. reported a drastic increase in the luminescence for the Mn^{2+}-doped $ZnAl_2O_4$ spinel when the annealing temperature was increased from 1200 to 1350 °C.[48] The improved crystallinity and lowering of antisite defects, which are known to provide additional pathways for nonradiative decays, may also result in increased UCL at higher annealing temperatures.[58] This is well supported by lifetime measurements. The green and red UC emissions for the sample annealed at 1400 °C were enhanced by 433 and 120 times the UC emissions obtained in the sample annealed at 1200 °C (Figure 7a). Thus, the modulation of phosphor's photophysical properties in terms of improved intensity and color tunability can be achieved by rational choice of codopant Mn^{2+} ion concentration and annealing temperature. Interestingly, the annealed samples showed very interesting color coordinated values (Figure S11) exhibiting the reverse color tunability of UC emissions from red to green on increasing the annealing temperature to 1400 °C. The color coordinates of the 1 mol % Mn^{2+} sample annealed at different temperatures are tabulated in the inset of Figure S11. The color is tuned from red to green, and hence, this material can act as a luminescence switch at different annealing temperatures.

The decay curves for ($^5F_4$,$^5S_2$) excited levels of Ho^{3+} ions (Figure 7b) show an increase in lifetime in 1300 °C annealing and decreases on further increase in annealing temperature as
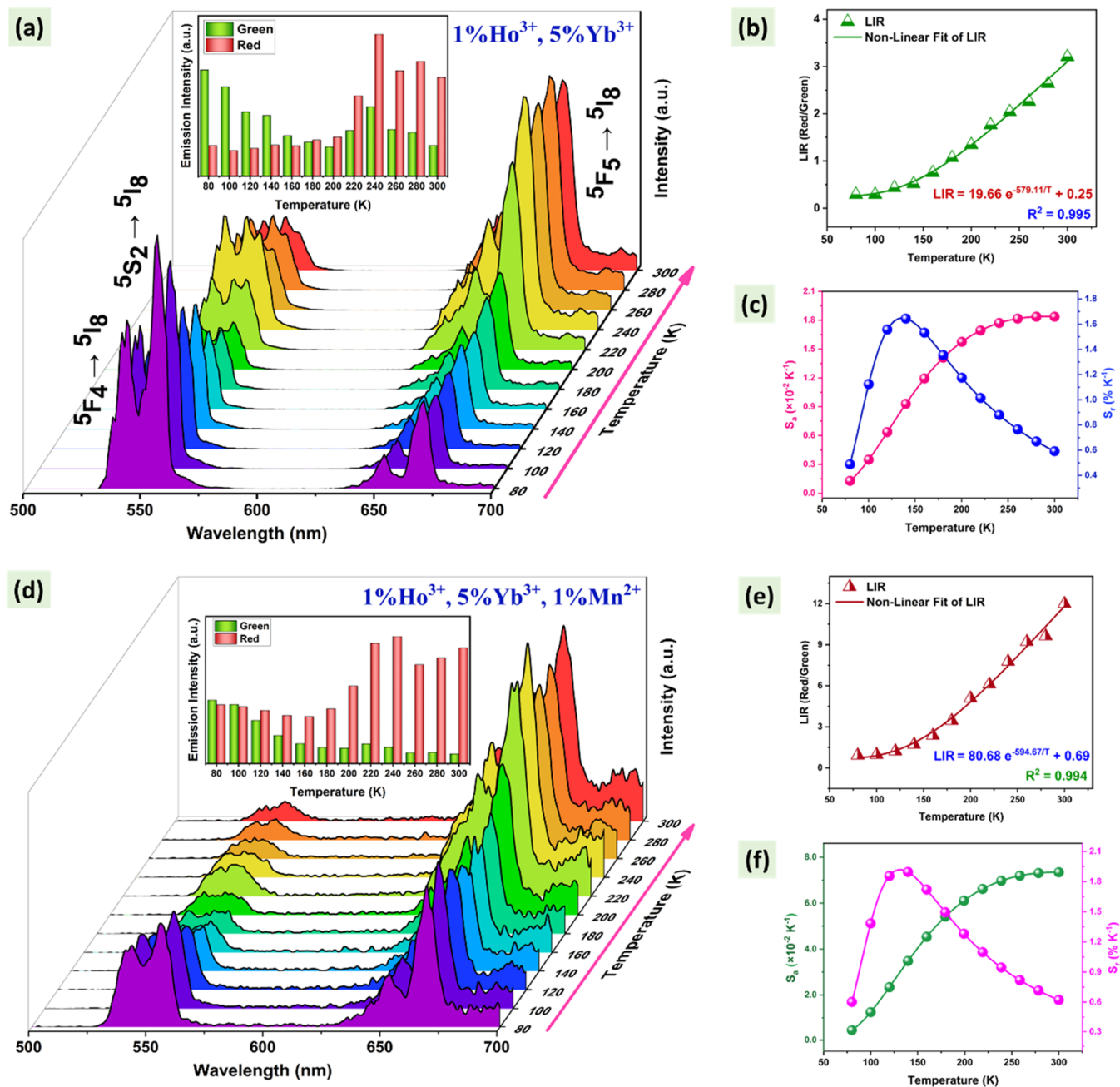
Figure 8. (a−c) Emission spectra, dependence of LIR for red and green UC emissions, and absolute and relative sensitivities at different temperatures from 80 to 300 K of ZnAl$_2$O$_4$:1%Ho^{3+},5%Yb^{3+} phosphor, (d−f) emission spectra, dependence of LIR for red and green UC emissions, and absolute and relative sensitivities as a function of temperature in the ZnAl$_2$O$_4$:1%Ho^{3+},5%Yb^{3+}, 1%Mn^{2+} sample under 980 nm laser excitation with 310 mW laser power, respectively.

shown in Figure 7d that could be a result of occurrence of ET and nonradiative processes. The decay curves of 1 mol % Mn^{2+} codoped ZnAl$_2$O$_4$: Ho^{3+},Yb^{3+} samples annealed at different temperatures for the $^5F_5$ level (Figure 7c) correspond well with the UCL emission studies as an increase in the lifetime values was observed. The lifetime values of red and green emissions for different 1 mol % Mn^{2+} samples annealed at different temperatures are tabulated in Table S7. The reduction of different defects such as oxygen vacancies and Zn$_{Al}$ antisite defects due to reduced cation inversion in the ZnAl$_2$O$_4$ lattice on annealing at high temperatures led to lowering of nonradiative decay routes. Annealing at high temperature usually increases the particle size and improves the crystallinity

of samples. Therefore, high-temperature annealing resulted in an increase in lifetime values of both red and green UC emissions. However, the lifetime of decay from ($^5F_4$,$^5S_2$) excited levels of Ho^{3+} ions decreased on higher temperature annealing at 1400 °C although the integral intensity was increased. The decreased lifetime revealed the increase in nonradiative decay processes from ($^5F_4$,$^5S_2$) excited levels.

3.4.6. Cryogenic Optical Thermometry Measurements. For a better understanding of change in the UC process that involves different mechanisms for each of the radiative transitions of Ho^{3+} ions as a function of temperature and to demonstrate the thermal sensing potential of our phosphor materials, we carried out a systematic temperature dependence
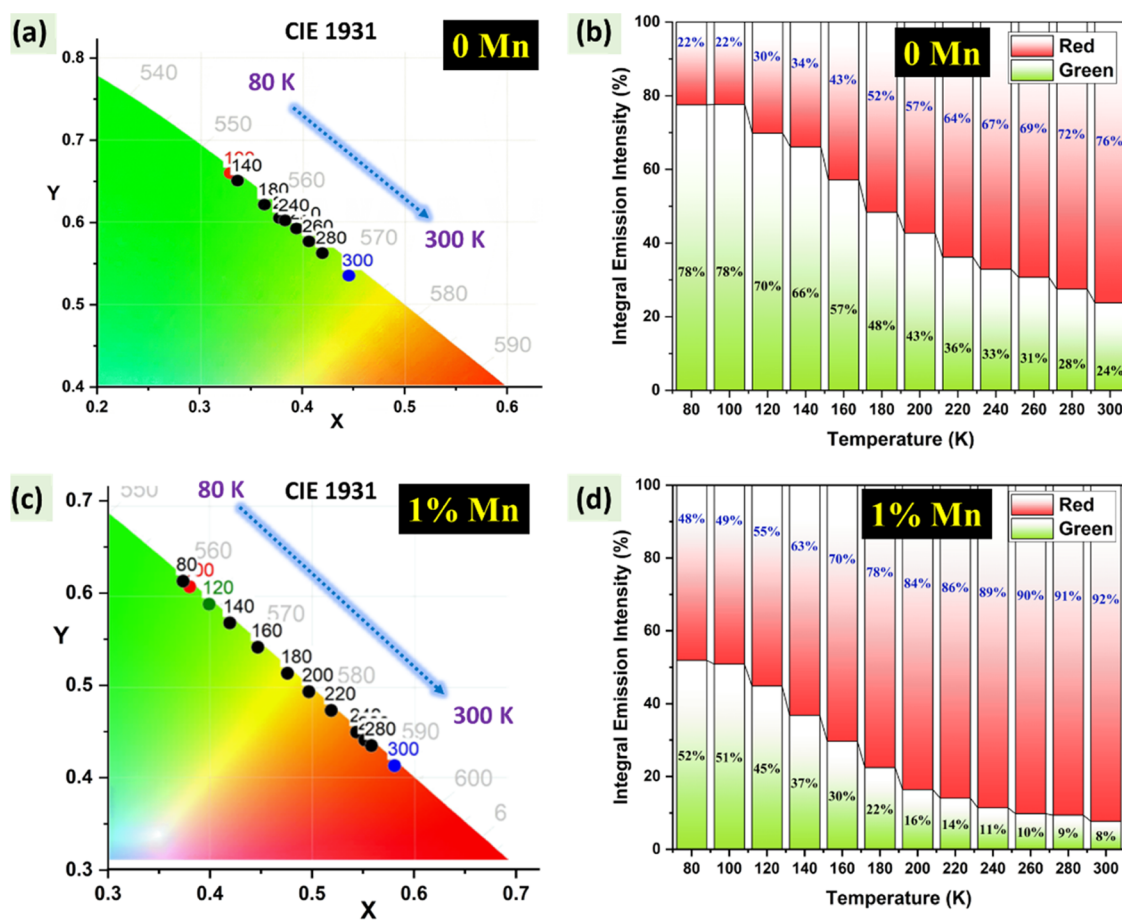
Figure 9. (a) CIE chromaticity diagrams, (b) percentage of green and red UC emission intensity in $ZnAl_2O_4$:1%Ho^{3+},5%Yb^{3+} at different temperatures, respectively, (c) CIE chromaticity diagrams, and (d) percentage of green and red UC emission intensities in the $ZnAl_2O_4$:1% Ho^{3+},5%Yb^{3+}, 1%Mn^{2+} phosphor as a function of temperature from 80 to 300 K, respectively, under a 980 nm laser excitation with 310 mW power.

analysis. We selected the $ZnAl_2O_4$:1%Ho^{3+}, 5%Yb^{3+} sample without Mn^{2+} codoping and with 1 mol % Mn^{2+} ions for temperature-dependent luminescence studies to get insights into the role of Mn^{2+} ions in thermal sensing as well as color tunability. The temperature-dependent UC emission spectra of both the samples were recorded over a temperature range of 80−300 K under 980 nm excitation, and the same is demonstrated with a three-dimensional (3D) model in Figure 8a,d. The variation in the green and red UC emission bands of Ho^{3+} ions can be explained by competitive temperature-dependent populating channels and decay pathways shown in Figure 4b. The relative red to green emission intensity ratios can be controlled by the presence of energy transfer pathways between Ho^{3+} and Yb^{3+} ions. From Figure 4b, it can be clearly understood that $(^5S_2, ^5F_4) \rightarrow ^5I_8$ and $^5F_5 \rightarrow ^5I_8$ and $(^3K_8, ^5F_2, ^5F_3) \rightarrow ^5I_7$ transitions of Ho^{3+} ions emit green and red UC emissions via radiative decay, respectively. The thermal population (TP) change is a well-reported process occurring between thermally coupled energy levels of Ho^{3+} ions where the occupation in the higher energy level increases at higher temperatures (Figure 4b).[41,59] As a consequence of the same, a significant enhancement in the $^5S_2 \rightarrow ^5I_8$ emission can be observed on cooling in both Mn^{2+} codoped and without Mn^{2+} codoped samples that suggests the quenching of $^5F_4 \rightarrow ^5I_8$ emission. The emission bands due to $^5S_2 \rightarrow ^5I_8$ and $^5F_4 \rightarrow ^5I_8$ transitions are well distinct in the UC emission spectrum of the sample without Mn^{2+} ions up to 160 K, and above 160 K, the

intensity ratios become similar, which suggests that TP becomes significant at temperatures higher than 160 K.

The multiphonon relaxation of excited Ho^{3+} ions in $(^5S_2, ^5F_4)$ energy levels and nonradiative decay processes are involved in populating the $^5F_5$ energy levels. Since both the pathways are sensitive to temperature, the effect of multiphonon relaxation and nonradiative relaxation will be more prominent on cooling. Usually, the red UC emission is relatively more intense at room temperature that can be ascribed to a greater number of possible channels for populating the $^5F_5$ energy levels of Ho^{3+} ions. As the multiphonon relaxation mode and nonradiative decay decrease with decreasing temperatures, the occupations of $^5F_5$ energy levels of Ho^{3+} ions are reduced as we move toward lower temperatures below room temperature. The same can be well understood from emission intensity ratios of green and red emitting bands at 80 K in the inset of Figure 8a,d, where the green emission is more intense than the red as the phonon coupling of the host matrix is deactivated at low temperatures.[39]

The presence of phonon-assisted ET between Ho^{3+} and Yb^{3+} ions along with ET between resonant levels to populate higher excited states can be very useful for the temperature-dependent luminescence.[60] In the sample without Mn^{2+} ions, the MPR, nonradiative decay, and Ho^{3+}−Yb^{3+} energy transfer channels occur simultaneously, and their dynamics can be changed on variation in temperature. The interesting finding of the

Table 1. Temperature Sensitivities and Temperature Range of Different Optical Thermometers Based on the Ln^{3+}-Doped Upconverting Phosphors

system	S_a maximum (K^{-1})	temp. range (K)	S_r maximum (% K^{-1})	ratio used	refs
$Na_3Y(VO_4)_2$: Ho^{3+}	0.010	298–618	0.51 (298 K)	$(^5F_4/^5S_2)$, $^5F_5 \rightarrow {}^5I_8$	61
$ZnWO_4$: Yb^{3+}, Ho^{3+}	0.0064 (83 K)	83–503		$^5F_4/^5S_2 \rightarrow {}^5I_8$, $^5I_7$	40
$La_2Mo_2O_9$:Yb^{3+}, Er^{3+}	0.010 (493 K)	293–553	1.15 (293 K)	$^2H_{11/2}$, $^4S_{3/2} \rightarrow {}^4I_{15/2}$	62
$La_2Mo_2O_9$: Yb^{3+}, Ho^{3+}	0.020		0.30 (293 K)		
$CaMoO_4$: Yb^{3+}, Ho^{3+}, Mg^{2+}	0.0066 (353 K)	303–543		$^3K_8$, $^5F_3 \rightarrow {}^5I_8$	60
$LiYF_4$:20Yb^{3+}, 1Ho^{3+}	0.0100 (159 K)	100–500	4.77 (500 K)	$^5F_5$, $(^5F_4/^5S_2) \rightarrow {}^5I_8$	41
KLu_2F_7:$Yb^{3+}/Er^{3+}/Mn^{2+}$	0.0451	303–543		$^4F_{9/2}$, $^4S_{3/2} \rightarrow {}^4I_{15/2}$	24
	0.0124			$^2H_{11/2}$, $^4S_{3/2} \rightarrow {}^4I_{15/2}$	
$Al_2Mo_3O_{12}$:$Ho^{3+}/0.26Yb^{3+}$	0.0291 (543 K)	303–543	0.465 (423 K)	$^5F_5$, $(^5F_4/^5S_2) \rightarrow {}^5I_8$	13
	0.1739 (543 K)		0.464 (423 K)	$^5F_5 \rightarrow {}^5I_8$ to $(^5F_4/^5S_2) \rightarrow {}^5I_7$	
$Na(Y, Gd)F_4$:30% Ho^{3+}		293–873	1.0 (300 K)	$^5F_5$, $(^5F_4/^5S_2) \rightarrow {}^5I_8$	39
$Er^{3+}/Ho^{3+}/Yb^{3+}$ codoped $Ba_2TiGe_2O_8$	0.00593	333–573	0.59 (573 K)	$^2H_{11/2}$, $^4S_{3/2} \rightarrow {}^4I_{15/2}$	38
$BaTiO_3$: Ho^{3+},Yb^{3+}	0.0095 (12 K)	12–300		$(^5F_4/^5S_2) \rightarrow {}^5I_8$	59
	0.0002 (300 K)				
$Na_{0.5}Bi_{0.5}TiO_3$:0.5 atom % Ho^{3+}	0.00009 (167 K)	167–377	6.14 (167 K)	$(^5F_4/^5S_2) \rightarrow {}^5I_8$	42
	0.00211 (377 K)		1.03 (377 K)		
$ZnAl_2O_4$:1%Ho^{3+},5%Yb^{3+}	0.01836 (300 K)	80–300	1.644 (140 K)	$^5F_5$, $(^5F_4/^5S_2) \rightarrow {}^5I_8$	this work
	0.00129 (80 K)		0.592 (300 K)		
$ZnAl_2O_4$:1%Ho^{3+},5%Yb^{3+},1%Mn^{2+}	0.0734 (300 K)	80–300	1.894 (140 K)	$^5F_5$, $(^5F_4/^5S_2) \rightarrow {}^5I_8$	this work
	0.00447 (80 K)		0.602 (300 K)		

temperature dependence studies is that the integrated green emission intensities show a decreasing trend in intensity till 200 K and then increases till 240 K followed by a decreasing trend on further rise in the temperature for both the samples. On the contrary, both the red UC emission bands at 652 and 669 nm increase up to 240 K, and then, a decreasing trend was observed. The above-mentioned observations may be attributed to different dominant decay processes at different temperature ranges. The competition between MPR, non-radiative decay, and ET processes results in the increase in red emission at the expense of green emission that decreases due to increased MPR processes as temperature increases. However, a sharp rise in the UC emission intensities of both red and green bands from 200 to 240 K may be due to thermally increased energy transfer pathways between Ho^{3+} and Yb^{3+} pairs.[13] However, a further rise in the temperature leads to thermal quenching as a consequence of enhanced nonradiative routes and also acts as an offset for ET routes. The increase in the 652 nm red emission band can be explained by thermal population change for $^3K_8$, $^5F_2$, and $^5F_3$ levels at high temperatures.

From the inset of Figure 8a, it can be inferred that the intensity of green $(^5F_4, ^5S_2) \rightarrow {}^5I_8$ emission is enhanced on cooling and that of red emission enhances on heating the sample without Mn^{2+} ions, and impressively, the UC emission spectra at 300 and 80 K appear to be opposite in terms of red and green UC emission intensities without much changes in peak positions. Hence, the LIR of red and green UC emissions (I_R/I_G) from electronically coupled states of Ho^{3+} ions was opted to explore the temperature dependence as the emissions from these levels are more sensitive to temperature changes. Since the R/G ratio increases with the increase in temperature, the dependence can be expressed in terms of the exponential equation[13]

$$LIR = \frac{I_R}{I_G} = A \exp(-B/T) + C \tag{4}$$

where I_R and I_G denote the luminescence intensities and A, B, and C represent constants. The temperature sensing performance of the $ZnAl_2O_4$:1%Ho^{3+}, 5%Yb^{3+} sample was estimated using the nonthermally coupled levels, and LIR values are found to be $19.66 \exp(-579.11/T) + 0.25$ (Figure 8b). As reported in the literature, the absolute sensitivity (S_a) and relative sensitivity (S_r) values were analyzed using the following relations[13,41]

$$S_a(K^{-1}) = \left| \frac{dLIR}{dT} \right| = A \exp(-B/T) \times B/T^2 \tag{5}$$

$$S_r(\%K^{-1}) = \frac{1}{LIR} \left| \frac{dLIR}{dT} \right| \times 100$$

$$= \frac{A \exp(-B/T)}{A \exp(-B/T) + C} \times \frac{B}{T^2} \times 100 \tag{6}$$

For the I_R/I_G, the S_a value of the $ZnAl_2O_4$:1%Ho^{3+}, 5%Yb^{3+} sample increases with temperature and attains a maximum value of 0.01836 K^{-1} at 300 K (Figure 8c). The S_a or rate of LIR change with temperature increased significantly up to 200 K and then increased gradually. Initially, LIR values showed a gradual increase with temperatures up to 160 K and then increases significantly with temperature. The above-mentioned fact resulted in the rise of the S_r value with a maximum value of 1.644% K^{-1} at 140 K and decrease on further rise in the temperature. Also, only slight color tunability from green to yellowish green was achieved without Mn^{2+} codoping on increasing the temperature as presented by the color coordinate diagram in Figure 9a and is supported by the percentage variation of green and red UC emission as a function of temperature as demonstrated by Figure 9b.

As the color tunability from red to green emission was obtained on codoping of Mn^{2+} ions, the temperature dependence analysis could be very useful in understanding the dynamics of different ET and nonradiative channels, especially at lower temperatures where the MPR and nonradiative routes are slowed down. In the 1 mol % Mn^{2+}

codoped sample, the ET between Mn^{2+} and Ho^{3+} ions induces extra energy transfer pathways relative to the sample without Mn^{2+} ions. As ET processes are sensitive to temperature, Mn^{2+} codoping leads to vigorous variation in the luminescence intensities that is required for a highly sensitive optical thermometer. Impressively, a stronger thermal dependence of LIR was observed for the phosphor with codoped Mn^{2+} ions (Figure 8e). The LIR versus temperature curve was fitted using the equation $80.68 \exp(-594.67/T) + 0.69$, and the S_a value increased with temperature and a maximum of 0.0734 K^{-1} at 300 K (Figure 8f). The S_r values show an increasing trend initially and reached a maximum value of 1.894% K^{-1} at 140 K and decreases on further rise in the temperature. To demonstrate the temperature uncertainty (ΔT), we have used the following expression

$$\Delta T = \frac{1}{S_r} \frac{\delta \text{LIR}}{\text{LIR}} \tag{7}$$

The relative error, i.e., $\delta\text{LIR}/\text{LIR}$, for temperature determination has been calculated as the uncertainty in experimental LIR and discussion is provided in Section S1. The ΔT values shown in Figure S12 were determined to be in between 0.03 and 0.11 K in the temperature range of 80−300 K, revealing high resolution for the temperature readout.

The sensitivity values of phosphors in this work are promising, and a relative comparison of similar upconversion phosphors reported in recent years is presented in Table 1. The sensitivity values of our phosphor material are relatively better than the reported Ho^{3+}/Yb^{3+}-based upconversion phosphors at 300 K and even at low temperature below RT. We could achieve a maximum S_a of 73.4×10^{-3} K^{-1} at 300 K, and even at 80 K, a higher S_a value of 4.47×10^{-3} K^{-1} was attained. In addition, a high S_r of 1.89% K^{-1} at 167 K and a S_r of 0.6% K^{-1} are still maintained till 300 K in the $ZnAl_2O_4{:}Ho^{3+},Yb^{3+},Mn^{2+}$ phosphor. A higher sensitivity in the Mn^{2+}-codoped phosphor can be attributed to the occurrence of energy transfer processes that can lead to significant variation in the red and green UC emissions by modulating the population channels for excited states of Ho^{3+} ions. Moreover, the phosphor with codoped Mn^{2+} ions exhibits a fascinating property of emission color shift from green to red region with the temperature rise from 80 to 300 K as depicted by the CIE color coordinate diagram in Figure 9c, which reflects the potential of $ZnAl_2O_4{:}$ Ho^{3+}, Yb^{3+}, Mn^{2+} phosphor for cryogenic region thermal sensing as well as rough temperature analysis by naked eyes. The percentage variation of green and red UC emissions of this phosphor as a function of temperature is demonstrated in Figure 9d. The complete change in the emission color at RT and cryogenic temperature can be utilized for safety signs directly observable by human eyes. This will broaden the scope of applications of Ho^{3+}-based phosphors for a wide range of advanced applications. To further emphasize the uniqueness of this work, we would like to emphasize that Mn^{2+} codoping with optimum concentration generates singular red emission, whereas high-temperature annealing brings back the green color emission. On the other hand, in situ thermal treatment from 80 to 300 K shows the color evolution from green to red, highlighting the significant potential of this material for temperature-based luminescence switching.

4. CONCLUSIONS

In this work, a series of $ZnAl_2O_4{:}1\%Ho^{3+},5\%Yb^{3+}, x\%Mn^{2+}$ (x = 0.25, 0.5, 1, and 2 mol %) phosphors were synthesized using the solid-state route. Their photophysical properties, energy transfer efficiencies, and two photon upconversion mechanisms for green and red UC emissions were extensively studied by time-resolved photoluminescence spectroscopy and laser power dependencies. Moreover, the modulation in luminescence properties manifested by incorporation of Mn^{2+} ions and a temperature-dependent investigation revealed the interesting temperature-sensitive color tunability of this phosphor material from 80 to 300 K. A singular red UC emission with 94% red emission is achieved by the $Ho^{3+}-Mn^{2+}$ energy transfer (ET) by adjusting the codoping concentration of Mn^{2+} ions. Moreover, the color tunability from red to green domains on higher temperature annealing exhibits the potential of our phosphor for luminescence switching. The inclusion of Mn^{2+} ions enhances the maximum S_a at 300 K by 4 times, and the maximum S_r and S_a of 1.89% K^{-1} (140 K) and 0.0734 K^{-1} (300 K) were obtained for the $ZnAl_2O_4{:}Ho^{3+}$, Yb^{3+}, Mn^{2+} sample, respectively. A high S_a of 0.00447 K^{-1} and S_r of 0.6025% K^{-1} were retained in the $ZnAl_2O_4{:}Ho^{3+}$, Yb^{3+}, Mn^{2+} sample even at a low temperature of 80 K. The presence of competitive multiphonon relaxations, nonradiative pathways, and initiating extra ET channels could be a promising strategy for enhancing the thermal sensitivities of Ln^{3+}-based luminescence thermometers. Furthermore, this phosphor displays potential for bioapplications as the single red emission is required for safer and highly sensitive optical imaging.

■ ASSOCIATED CONTENT

Ⓢ Supporting Information

The Supporting Information is available free of charge at https://pubs.acs.org/doi/10.1021/acsomega.3c03629.

> XRD pattern of high temperature-annealed (1200−1400 °C) $ZnAl_2O_4{:}1\%Ho^{3+},5\%Yb^{3+},1\%Mn^{2+}$ and $Yb_2O_3{:}1\%$ Ho^{3+} annealed at 1200 °C; XPS survey scan of the Mn core level; EPR spectra (RT and 100 K) and g-value table of different concentrations of Mn^{2+} codoping and that of high temperature-annealed $ZnAl_2O_4{:}1\%Ho^{3+},5\%$ Yb^{3+}; positron annihilation spectra and lifetime table; red/green integral area ratio table of all the samples; comparison of UC emission spectra of 1 mol % Ho^{3+} ion-doped Yb_2O_3 and $ZnAl_2O_4{:}1\%Ho^{3+}$, $5\%Yb^{3+}$ samples; color coordinates at different laser powers; UC lifetime values for 550 and 669 nm; UC emission spectra; CIE diagram and lifetime values at high annealing temperature; and discussion on LIR values with uncertainty determination and calculated values of $FIR_{(exp.)}$ and $\delta\text{LIR}/\text{LIR}$ from 80 to 300 K (PDF)

■ AUTHOR INFORMATION

Corresponding Author

Santosh Kumar Gupta − *Homi Bhabha National Institute, Mumbai 400094, India; Radiochemistry Division, Bhabha Atomic Research Centre, Mumbai 400085, India;* ⓞ orcid.org/0000-0002-1178-0159; Email: santoshg@ barc.gov.in, santufrnd@gmail.com

Authors

Annu Balhara − *Homi Bhabha National Institute, Mumbai 400094, India; Radiochemistry Division, Bhabha Atomic Research Centre, Mumbai 400085, India*

Anil Krishna Debnath − *Homi Bhabha National Institute, Mumbai 400094, India; Technical Physics Division, Bhabha Atomic Research Centre, Mumbai 400085, India*

Kathi Sudarshan − *Homi Bhabha National Institute, Mumbai 400094, India; Radiochemistry Division, Bhabha Atomic Research Centre, Mumbai 400085, India*

Complete contact information is available at:
https://pubs.acs.org/10.1021/acsomega.3c03629

Notes

The authors declare no competing financial interest.

■ REFERENCES

(1) Chen, G.; Qiu, H.; Prasad, P. N.; Chen, X. Upconversion Nanoparticles: Design, Nanochemistry, and Applications in Theranostics. *Chem. Rev.* **2014**, *114*, 5161−5214.

(2) Cheng, X.; Zhou, J.; Yue, J.; Wei, Y.; Gao, C.; Xie, X.; Huang, L. Recent Development in Sensitizers for Lanthanide-Doped Upconversion Luminescence. *Chem. Rev.* **2022**, *122*, 15998−16050.

(3) Dong, H.; Sun, L.-D.; Yan, C.-H. Local Structure Engineering in Lanthanide-Doped Nanocrystals for Tunable Upconversion Emissions. *J. Am. Chem. Soc.* **2021**, *143*, 20546−20561.

(4) Du, K.; Feng, J.; Gao, X.; Zhang, H. Nanocomposites based on lanthanide-doped upconversion nanoparticles: diverse designs and applications. *Light: Sci. Appl.* **2022**, *11*, No. 222.

(5) Guo, S.; Xie, X.; Huang, L.; Huang, W. Sensitive Water Probing through Nonlinear Photon Upconversion of Lanthanide-Doped Nanoparticles. *ACS Appl. Mater. Interfaces* **2016**, *8*, 847−853.

(6) Gupta, S. K.; Kadam, R. M.; Pujari, P. K. Lanthanide spectroscopy in probing structure-property correlation in multi-site photoluminescent phosphors. *Coord. Chem. Rev.* **2020**, *420*, No. 213405.

(7) Pokhrel, M.; Gupta, S. K.; Perez, A.; Modak, B.; Modak, P.; Lewis, L. A.; Mao, Y. Up- and Down-Convertible LaF$_3$:Yb,Er Nanocrystals with a Broad Emission Window from 350 nm to 2.8 μm: Implications for Lighting Applications. *ACS Appl. Nano Mater.* **2021**, *4*, 13562−13572.

(8) Wen, S.; Zhou, J.; Zheng, K.; Bednarkiewicz, A.; Liu, X.; Jin, D. Advances in highly doped upconversion nanoparticles. *Nat. Commun.* **2018**, *9*, No. 2415.

(9) Zhang, Z.; Han, Q.; Lau, J. W.; Xing, B. Lanthanide-Doped Upconversion Nanoparticles Meet the Needs for Cutting-Edge Bioapplications: Recent Progress and Perspectives. *ACS Mater. Lett.* **2020**, *2*, 1516−1531.

(10) Ge, X.; Wang, Z.; Bai, X.; Xu, H.; Fu, Z. Silicate Phosphors BaGa$_2$Si$_2$O$_8$:Ln^{3+} (Er^{3+}, Ho^{3+}, Yb^{3+}) Equipped with Intrinsic Optical Bistability toward Photonic Barcodes. *J. Phys. Chem. C* **2022**, *126*, 18839−18848.

(11) Rohilla, P.; Rao, A. S. Linear and non-linear photoluminescence studies of Ho^{3+}/Yb^{3+} co-doped titanate phosphors for photonic applications. *J. Alloys Compd.* **2022**, *928*, No. 167156.

(12) Jiang, X.; Zhang, Z.; Zhang, T.; Li, C.; Leng, Z.; Yang, W.; Wang, X.; Shi, X.; Zhang, X.; Sha, H.; Zhou, Z.; Lin, H.; Huang, K.; Li, C.; Su, Z.; Zeng, F. Enhanced up-conversion luminescence intensity of NaY(MoO$_4$)$_2$: Ho^{3+}/Yb^{3+} phosphor by doping with Mg^{2+} ions for use in high-efficiency optical temperature sensor. *J. Lumin.* **2022**, *245*, No. 118759.

(13) Lv, H.; Luo, L.; Li, W.; Du, P. Manipulating Upconversion Emission and Thermochromic Properties of Ho^{3+}/Yb^{3+}-Codoped Al$_2$Mo$_3$O$_{12}$ Microparticles by Negative Lattice Expansion for Multimode Visual Optical Thermometry. *Inorg. Chem.* **2022**, *61*, 11442−11453.

(14) Bi, S.; Deng, Z.; Huang, J.; Wen, X.; Zeng, S. NIR-II Responsive Upconversion Nanoprobe with Simultaneously Enhanced Single-Band Red Luminescence and Phase/Size Control for Bioimaging and Photodynamic Therapy. *Adv. Mater.* **2023**, *35*, No. 2207038.

(15) Giordano, L.; Du, H.; Castaing, V.; Luan, F.; Guo, D.; Viana, B. Enhanced red-UC luminescence through Ce3+ co-doping in NaBiF$_4$:Yb^{3+}/Ho^{3+}(Er^{3+})/Ce^{3+} phosphors prepared by ultrafast coprecipitation approach. *Opt. Mater.: X* **2022**, *16*, No. 100199.

(16) Rai, M.; Singh, S. K.; Singh, A. K.; Prasad, R.; Koch, B.; Mishra, K.; Rai, S. B. Enhanced Red Upconversion Emission, Magnetoluminescent Behavior, and Bioimaging Application of NaSc$_{0.75}$Er$_{0.02}$Yb$_{0.18}$Gd$_{0.05}$F$_4$@AuNPs Nanoparticles. *ACS Appl. Mater. Interfaces* **2015**, *7*, 15339−15350.

(17) Srivastava, B. B.; Gupta, S. K.; Mao, Y. Single red emission from upconverting ZnGa$_2$O$_4$:Yb,Er nanoparticles co-doped by Cr^{3+}. *J. Mater. Chem. C* **2020**, *8*, 6370−6379.

(18) Wu, Y.; Lin, S.; Liu, J.; Ji, Y.; Xu, J.; Xu, L.; Chen, K. Efficient up-conversion red emission from TiO$_2$:Yb,Er nanocrystals. *Opt. Express* **2017**, *25*, 22648−22657.

(19) Tian, G.; Gu, Z.; Zhou, L.; Yin, W.; Liu, X.; Yan, L.; Jin, S.; Ren, W.; Xing, G.; Li, S.; Zhao, Y. Mn^{2+} Dopant-Controlled Synthesis of NaYF$_4$:Yb/Er Upconversion Nanoparticles for in vivo Imaging and Drug Delivery. *Adv. Mater.* **2012**, *24*, 1226−1231.

(20) DesMarias, T. L.; Costa, M. Mechanisms of chromium-induced toxicity. *Curr. Opin. Toxicol.* **2019**, *14*, 1−7.

(21) Gupta, S. K.; Kadam, R.; Natarajan, V.; Godbole, S. Nanoparticles of Sr$_{0.995}$Gd$_{0.005}$ZrO$_3$-gel-combustion synthesis, characterization, fluorescence and EPR spectroscopy. *Mater. Sci. Eng., B* **2014**, *183*, 6−11.

(22) Lu, H.; Hao, H.; Zhu, H.; Shi, G.; Fan, Q.; Song, Y.; Wang, Y.; Zhang, X. Enhancing temperature sensing behavior of NaLuF$_4$:Yb^{3+}/Er^{3+} via incorporation of Mn^{2+} ions resulting in a closed energy transfer. *J. Alloys Compd.* **2017**, *728*, 971−975.

(23) Nayak, P.; Nanda, S. S.; Pattnaik, S.; Rai, V. K.; Sharma, R. K.; Dash, S. Yb-Mn dimer tailored upconversion luminescence in CaWO$_4$:Er^{3+}/Yb^{3+}/Mn^{2+} green phosphors for thermometry and optical heating. *Opt. Laser Technol.* **2023**, *159*, No. 108990.

(24) Peng, Y.; Cheng, Z.; Khan, W. U.; Liu, T.; Shen, M.; Yang, S.; Zhang, Y. Enhancing upconversion emissions and temperature sensing properties by incorporating Mn^{2+} for KLu$_2$F$_7$:Yb^{3+}/Er^{3+} nanocrystals based on thermally and non-thermally coupled levels. *New J. Chem.* **2021**, *45*, 3876−3885.

(25) Ren, H.; Yang, F. Influence of Mn^{2+} on the up-conversion emission performance of Mn^{2+}, Yb^{3+}, Er^{3+}: ZnWO$_4$ green phosphors. *J. Mater. Sci.: Mater. Electron.* **2018**, *29*, 15396−15403.

(26) Szczeszak, A.; Grzyb, T.; Nowaczyk, G.; Ekner-Grzyb, A. Emission colour changes in the CaF$_2$ sub-microspheres doped with Yb^{3+}, Er^{3+} and Mn^{2+} ions. *J. Alloys Compd.* **2020**, *817*, No. 152718.

(27) Yuan, M.; Wang, R.; Zhang, C.; Yang, Z.; Yang, X.; Han, K.; Ye, J.; Wang, H.; Xu, X. Revisiting the Enhanced Red Upconversion Emission from a Single β-NaYF$_4$:Yb/Er Microcrystal By Doping with Mn^{2+} Ions. *Nanoscale Res. Lett.* **2019**, *14*, No. 103.

(28) Zhou, B.; Xu, B.; He, H.; Gu, Z.; Tang, B.; Ma, Y.; Zhai, T. Enhanced green upconversion luminescence in tetrahedral LiYF$_4$:Yb/Er nanoparticles by manganese(ii)-doping: the key role of the host lattice. *Nanoscale* **2018**, *10*, 2834−2840.

(29) Qiang, Q.; Wang, Y. Enhanced optical temperature sensing and upconversion emissions based on the Mn^{2+} codoped NaGdF$_4$:Yb^{3+},Ho^{3+} nanophosphor. *New J. Chem.* **2019**, *43*, 5011−5019.

(30) Zhu, Q.; Song, C.; Li, X.; Sun, X.; Li, J.-G. Up-conversion monodispersed spheres of NaYF$_4$:Yb^{3+}/Er^{3+}: green and red emission tailoring mediated by heating temperature, and greatly enhanced luminescence by Mn^{2+} doping. *Dalton Trans.* **2018**, *47*, 8646−8655.

(31) Chen, Z. T.; Song, E. H.; Wu, M.; Ding, S.; Ye, S.; Zhang, Q. Y. Bidirectional energy transfer induced single-band red upconversion emission of Ho^{3+} in KZnF$_3$:Mn^{2+},Yb^{3+},Ho^{3+} nanocrystals. *J. Alloys Compd.* **2016**, *667*, 134−140.

(32) Qiang, Q.; Wang, Y. Effect of Mn^{2+} on Upconversion Emission, Thermal Sensing and Optical Heater Behavior of Yb^{3+} - Er^{3+} Codoped NaGdF$_4$ Nanophosphors. *Front. Chem.* **2019**, *7*, No. 425.

(33) Reddy, K. L.; Rai, M.; Prabhakar, N.; Arppe, R.; Rai, S. B.; Singh, S. K.; Rosenholm, J. M.; Krishnan, V. Controlled synthesis, bioimaging and toxicity assessments in strong red emitting Mn^{2+} doped NaYF$_4$:Yb^{3+}/Ho^{3+} nanophosphors. *RSC Adv.* **2016**, *6*, 53698−53704.

(34) Zhang, Z.; Yang, W.; Jiang, X.; Geng, S.; Zhang, X.; Zhang, T.; Wang, X.; shi, X.; Leng, Z.; Lin, H.; Huang, K.; Li, C.; Zeng, F.; Su, Z. Influence of Mn^{2+} ions on the structure and spectral properties of BaY$_2$F$_8$:Yb^{3+}/Ho^{3+} phosphors. *J. Mater. Sci.: Mater. Electron.* **2022**, *33*, 21148−21160.

(35) Ajithkumar, G.; Yoo, B.; Goral, D. E.; Hornsby, P. J.; Lin, A.-L.; Ladiwala, U.; Dravid, V. P.; Sardar, D. K. Multimodal bioimaging using a rare earth doped Gd$_2$O$_2$S:Yb/Er phosphor with upconversion luminescence and magnetic resonance properties. *J. Mater. Chem. B* **2013**, *1*, 1561−1572.

(36) Park, J. Y.; Baek, M. J.; Choi, E. S.; Woo, S.; Kim, J. H.; Kim, T. J.; Jung, J. C.; Chae, K. S.; Chang, Y.; Lee, G. H. Paramagnetic Ultrasmall Gadolinium Oxide Nanoparticles as Advanced T1 MRI Contrast Agent: Account for Large Longitudinal Relaxivity, Optimal Particle Diameter, and In Vivo T1 MR Images. *ACS Nano* **2009**, *3*, 3663−3669.

(37) Jahanbazi, F.; Mao, Y. Recent advances on metal oxide-based luminescence thermometry. *J. Mater. Chem. C* **2021**, *9*, 16410−16439.

(38) Hou, B.; Jia, M.; Li, P.; Liu, G.; Sun, Z.; Fu, Z. Multifunctional Optical Thermometry Based on the Rare-Earth-Ions-Doped Up-/Down-Conversion Ba$_2$TiGe$_2$O$_8$:Ln (Ln = Eu^{3+}/ Er^{3+}/ Ho^{3+}/ Yb^{3+}) Phosphors. *Inorg. Chem.* **2019**, *58*, 7939−7946.

(39) van Swieten, T. P.; Yu, D.; Yu, T.; Vonk, S. J. W.; Suta, M.; Zhang, Q.; Meijerink, A.; Rabouw, F. T. A Ho^{3+}-Based Luminescent Thermometer for Sensitive Sensing over a Wide Temperature Range. *Adv. Opt. Mater.* **2021**, *9*, No. 2001518.

(40) Chai, X.; Li, J.; Wang, X.; Li, Y.; Yao, X. Upconversion luminescence and temperature-sensing properties of Ho^{3+}/Yb^{3+}-codoped ZnWO$_4$ phosphors based on fluorescence intensity ratios. *RSC Adv.* **2017**, *7*, 40046−40052.

(41) Li, W.; Hu, L.; Chen, W.; Sun, S.; Guzik, M.; Boulon, G. The effect of temperature on green and red upconversion emissions of LiYF$_4$:20Yb^{3+},1Ho^{3+} and its application for temperature sensing. *J. Alloys Compd.* **2021**, *866*, No. 158813.

(42) Wang, Y.; Wang, Y.; Ma, C.; Feng, Z.; Zuo, C.; Ye, W.; Zhao, C.; Li, Y.; Wen, Z.; Cao, Z.; Cao, Z.; Shen, X.; Wang, C.; Li, Y.; Yuan, X.; Cao, Y. Excellent cryogenic optical thermometry based on green up-conversion of Ho^{3+}-doped perovskite Na$_{0.5}$Bi$_{0.5}$TiO$_3$ ceramics. *J. Mater. Chem. C* **2021**, *9*, 1353−1361.

(43) Kumar, M.; Gupta, S. K. An insight into optical spectroscopy of intense green emitting ZnAl$_2$O$_4$:Tb^{3+} nanoparticles: photo, thermally stimulated luminescence and EPR study. *J. Lumin.* **2015**, *168*, 151−157.

(44) Pathak, N.; Gupta, S. K.; Sanyal, K.; Kumar, M.; Kadam, R. M.; Natarajan, V. Photoluminescence and EPR studies on Fe^{3+} doped ZnAl$_2$O$_4$: an evidence for local site swapping of Fe^{3+} and formation of inverse and normal phase. *Dalton Trans.* **2014**, *43*, 9313−9323.

(45) Rojas-Hernandez, R. E.; Rubio-Marcos, F.; Romet, I.; del Campo, A.; Gorni, G.; Hussainova, I.; Fernandez, J. F.; Nagirnyi, V. Deep-Ultraviolet Emitter: Rare-Earth-Free ZnAl$_2$O$_4$ Nanofibers via a Simple Wet Chemical Route. *Inorg. Chem.* **2022**, *61*, 11886−11896.

(46) Olsen, J. V.; Kirkegaard, P.; Pedersen, N. J.; Eldrup, M. PALSfit: A new program for the evaluation of positron lifetime spectra. *Phys. Status Solidi C* **2007**, *4*, 4004−4006.

(47) Zhao, D.; Zhu, S.-Y.; Zhang, R.-J.; Yao, Q.-X.; Liu, W.; Xue, Y.-L. Designing a Polyphosphate Polymorph of CsMg(PO$_3$)$_3$ as Host Lattice for Preparing Single Mn^{2+}-Oxidation Doped Phosphor in the Open Environment. *Inorg. Chem.* **2021**, *60*, 17942−17951.

(48) Cornu, L.; Duttine, M.; Gaudon, M.; Jubera, V. Luminescence switch of Mn-Doped ZnAl$_2$O$_4$ powder with temperature. *J. Mater. Chem. C* **2014**, *2*, 9512−9522.

(49) Singh, V.; Chakradhar, R. P. S.; Rao, J. L.; Kim, D.-K. Characterization, EPR and luminescence studies of ZnAl$_2$O$_4$:Mn phosphors. *J. Lumin.* **2008**, *128*, 394−402.

(50) Balhara, A.; Gupta, S. K.; Patra, G. D.; Modak, B.; Prakash, J.; Sudarshan, K.; Mohapatra, M. Stabilization of Eu^{2+} in Li$_2$B$_4$O$_7$ with the BO$_3$ network through U^{6+} co-doping and defect engineering. *Phys. Chem. Chem. Phys.* **2023**, *25*, 1889−1902.

(51) Bezkrovnyi, O.; Małecka, M. A.; Lisiecki, R.; Ostroushko, V.; Thomas, A. G.; Gorantla, S.; Kepinski, L. The effect of Eu doping on the growth, structure and red-ox activity of ceria nanocubes. *CrystEngComm* **2018**, *20*, 1698−1704.

(52) Sudarshan, K.; Sharma, S. K.; Gupta, R.; Gupta, S. K.; Sayed, F. N.; Pujari, P. K. Role of surface defects in catalytic properties of CeO$_2$ nanoparticles towards oxygen reduction reaction. *Mater. Chem. Phys.* **2017**, *200*, 99−106.

(53) Jia, H.; Liu, Z.; Liao, L.; Gu, Y.; Ding, C.; Zhao, J.; Zhang, W.; Hu, X.; Feng, X.; Chen, Z.; Liu, X.; Qiu, J. Upconversion Luminescence from Ln^{3+}(Ho^{3+},Pr^{3+}) Ion-Doped BaCl$_2$ Particles via NIR Light of Sun Excitation. *J. Phys. Chem. C* **2018**, *122*, 9606−9610.

(54) Li, K.; Deun, R. V. Low-Temperature Solid-State Synthesis and Upconversion Luminescence Properties in (Na/Li)Bi-(MoO$_4$)$_2$:Yb^{3+},Er^{3+} and Color Tuning in (Na/Li)Bi-(MoO$_4$)$_2$:Yb^{3+},Ho^{3+},Ce^{3+} Phosphors. *Inorg. Chem.* **2019**, *58*, 6821−6831.

(55) Suo, H.; Guo, C.; Wang, W.; Li, T.; Duan, C.; Yin, M. Mechanism and stability of spectrally pure green up-conversion emission in Yb^{3+}/Ho^{3+} co-doped Ba$_5$Gd$_8$Zn$_4$O$_{21}$ phosphors. *Dalton Trans.* **2016**, *45*, 2629−2636.

(56) Sontakke, A. D.; van Bunningen, A. J.; Rabouw, F. T.; Meijers, S.; Meijerink, A. Unraveling the Eu^{2+} → Mn^{2+} Energy Transfer Mechanism in w-LED Phosphors. *J. Phys. Chem. C* **2020**, *124*, 13902−13911.

(57) Wu, M.; Jiang, X. F.; Song, E. H.; Su, J.; Chen, Z. T.; Dai, W. B.; Ye, S.; Zhang, Q. Y. Tailoring the upconversion of ABF$_3$:Yb^{3+}/Er^{3+} through Mn^{2+} doping. *J. Mater. Chem. C* **2016**, *4*, 9598−9607.

(58) Pathak, N.; Ghosh, P. S.; Saxena, S.; Dutta, D.; Yadav, A. K.; Bhattacharyya, D.; Jha, S. N.; Kadam, R. M. Exploring Defect-Induced Emission in ZnAl$_2$O$_4$: An Exceptional Color-Tunable Phosphor Material with Diverse Lifetimes. *Inorg. Chem.* **2018**, *57*, 3963−3982.

(59) Mahata, M. K.; Koppe, T.; Kumar, K.; Hofsäss, H.; Vetter, U. Upconversion photoluminescence of Ho^{3+}-Yb^{3+} doped barium titanate nanocrystallites: Optical tools for structural phase detection and temperature probing. *Sci. Rep.* **2020**, *10*, No. 8775.

(60) Dey, R.; Kumari, A.; Soni, A. K.; Rai, V. K. CaMoO$_4$:Ho^{3+}−Yb^{3+}−Mg^{2+} upconverting phosphor for application in lighting devices and optical temperature sensing. *Sens. Actuators, B* **2015**, *210*, 581−588.

(61) Lv, L.; Wu, X.; Xiao, Q.; Yin, X.; Fan, Y.; Dong, X.; Xu, X.; Luo, X. Up-conversion luminescence and temperature sensing properties of Ho^{3+} activated Na$_3$Y(VO$_4$)$_2$ phosphors under 980 and 808 nm excitation. *J. Lumin.* **2023**, *257*, No. 119739.

(62) Xiao, Q.; Dong, X.; Yin, X.; Wang, H.; Zhong, H.; Liu, K.; Dong, B.; Luo, X. Promising Yb^{3+}-sensitized La$_2$Mo$_2$O$_9$ phosphors for multi-color up-conversion luminescence and optical temperature sensing. *J. Alloys Compd.* **2022**, *895*, No. 162686.